

# NAVAL POSTGRADUATE SCHOOL Monterey, California



## THESIS

### **CREEP BEHAVIOR OF THE INTERFACE REGION IN CONTINUOUS FIBER REINFORCED METAL-MATRIX COMPOSITES**

by

John V. Funn

September, 1997

Thesis Advisor:

Indranath Dutta

Approved for public release; distribution is unlimited.

DTIC QUALITY INSPECTED 3

19980414 048

REPORT DOCUMENTATION PAGE			Form Approved OMB No. 0704-0188	
Public reporting burden for this collection of information is estimated to average 1 hour per response, including the time for reviewing instruction, searching existing data sources, gathering and maintaining the data needed, and completing and reviewing the collection of information. Send comments regarding this burden estimate or any other aspect of this collection of information, including suggestions for reducing this burden, to Washington Headquarters Services, Directorate for Information Operations and Reports, 1215 Jefferson Davis Highway, Suite 1204, Arlington, VA 22202-4302, and to the Office of Management and Budget, Paperwork Reduction Project (0704-0188) Washington DC 20503				
1. AGENCY USE ONLY (Leave blank)		2. REPORT DATE September 1997		3. REPORT TYPE AND DATES COVERED Master's Thesis
4. TITLE AND SUBTITLE Creep Behavior of the Interface Region in Continuous Fiber Reinforced Metal-Matrix Composites			5. FUNDING NUMBERS	
6. Author: Lieutenant John Vincent Funn				
7. PERFORMING ORGANIZATION NAME(S) AND ADDRESS(ES) Naval Postgraduate School Monterey CA 93943-5000			8. PERFORMING ORGANIZATION REPORT NUMBER	
9. SPONSORING/MONITORING AGENCY NAME(S) AND ADDRESS(ES)			10. SPONSORING/MONITORING AGENCY REPORT NUMBER	
11. SUPPLEMENTARY NOTES The views expressed in this thesis are those of the author and do not reflect the official policy or position of the Department of Defense or the U.S. Government				
12a. DISTRIBUTION/AVAILABILITY STATEMENT Approved for public release; distribution is unlimited.			12b. DISTRIBUTION CODE	
13. ABSTRACT (maximum 200 words)  The accurate incorporation of interface effects on creep in metal matrix composites is contingent on the direct experimental determination of the deformation kinetics. The goal is accomplished by isolating the composite interface and precisely measuring the creep characteristics of the interface, by utilizing a fiber-pushout apparatus to apply a constant force on the fiber of a model single fiber composite (SFC), so that the interface can creep under the applied shear stress. Two different model fiber-matrix systems - one with no mutual solubility and the other with limited mutual solubility - were investigated. In both systems, the interface displayed Bingham flow (diffusional flow with a threshold stress). The Finite Element Method (FEM) was utilized to check the conceptual validity of the test approach for one of the model systems, and to provide insight into the design of the sample and test apparatus. FEM was also utilized to estimate the residual radial stresses present in the model composite system following cooling from an elevated to ambient temperature. Based on the experimental results and the FEM analysis, an analytical model is advanced to incorporate the effect of radial residual stresses on the creep of the fiber-matrix interface. The model yields an explicit constitutive law which describes the stress, temperature, and matrix property dependence of interfacial creep. The model also indicates that the experimentally observed threshold stress is directly attributable to the radial stress acting on the fiber-matrix interface.				
14. SUBJECT TERMS Composite, Interface, Creep			15. NUMBER OF PAGES 107	
			16. PRICE CODE	
17. SECURITY CLASSIFICATION OF REPORT Unclassified	18. SECURITY CLASSIFICATION OF THIS PAGE Unclassified	19. SECURITY CLASSIFICATION OF ABSTRACT Unclassified	20. LIMITATION OF ABSTRACT UL	



Approved for public release; distribution is unlimited.

# **CREEP BEHAVIOR OF THE INTERFACE REGION IN CONTINUOUS FIBER REINFORCED METAL-MATRIX COMPOSITES**

John V. Funn  
Lieutenant, United States Navy  
B.S., Cornell University, 1990

Submitted in partial fulfillment  
of the requirements for the degree of

**MASTER OF SCIENCE IN MECHANICAL ENGINEERING**

from the

**NAVAL POSTGRADUATE SCHOOL**

**September 1997**

Author:



John V. Funn

Approved by:



Indranath Dutta, Thesis Advisor



T. R. McNelley, Chairman  
Department of Mechanical Engineering



## ABSTRACT

The accurate incorporation of interface effects on creep in metal matrix composites is contingent on the direct experimental determination of the deformation kinetics. An experimental approach is identified that is capable of providing the necessary data regarding interface deformation without being influenced by the other mechanisms in the composite. The goal is accomplished by isolating the composite interface and precisely measuring the creep characteristics of the interface, by utilizing a fiber-pushout apparatus to apply a constant force on the fiber of a model single fiber composite (SFC), so that the interface can creep under the applied shear stress. Two different model fiber-matrix systems - one with no mutual solubility and the other with limited mutual solubility - were investigated. In both systems, the interface displayed Bingham flow (diffusional flow with a threshold stress). The Finite Element Method (FEM) was utilized to check the conceptual validity of the test approach for one of the model systems, and to provide insight into the design of the sample and test apparatus. FEM was also utilized to estimate the residual radial stresses present in the model composite system following cooling from an elevated to ambient temperature. Based on the experimental results and the FEM analysis, an analytical model is advanced to incorporate the effect of radial residual stresses on the creep of the fiber-matrix interface. The model yields an explicit constitutive law which describes the stress, temperature, and matrix property dependence of interfacial creep. The model also indicates that the experimentally observed threshold stress is directly attributable to the normal (radial) stress acting on the fiber-matrix interface.



## TABLE OF CONTENTS

I.	INTRODUCTION .....	1
II.	BACKGROUND .....	5
A.	SOME OBSERVATIONS ON COMPOSITE CREEP .....	5
B.	COMPOSITE CREEP MODELS .....	9
C.	THE CASE FOR STUDYING INTERFACE CREEP .....	14
III.	OBJECTIVES .....	21
IV.	EXPERIMENTAL .....	23
A.	COMPOSITE SYSTEMS .....	23
B.	SINGLE FIBER COMPOSITES .....	27
1.	Fabrication .....	27
2.	Specimen Preparation for Pushout/Creep Testing .....	28
a.	Sectioning .....	28
b.	Mounting .....	28
3.	Mechanical Testing and Microscopic Examination .....	29
a.	Apparatus .....	29
b.	Pushout Testing .....	30
c.	Creep Testing .....	33
C.	DIRECT OBSERVATION OF INTERFACIAL SLIDING .....	34
1.	Fabrication .....	34
2.	Specimen Preparation .....	34
a.	Sectioning and Polishing .....	34
b.	Carbon Grid Deposition .....	35
3.	Testing and Microscopic Examination .....	36
D.	DATA ACQUISITION .....	37
IV.	EXPERIMENTAL RESULTS .....	39
A.	DIRECT OBSERVATION OF INTERFACIAL SLIDING .....	39
B.	PUSHOUT TESTING .....	42
1.	Lead-Quartz System Pushout Tests .....	42
2.	Lead-Nickel System Pushout Tests .....	44
3.	Pushout Test Summary .....	49
C.	CREEP RESPONSE OF THE INTERFACE .....	49
1.	Lead-Quartz SFC Creep Response .....	50
2.	Lead-Nickel SFC Creep Response .....	54
D.	ANALYSIS OF CREEP RESPONSE .....	57
V.	EVALUATION OF THE VALIDITY OF THE EXPERIMENTAL APPROACH: FINITE ELEMENT MODEL .....	63
A.	PURPOSE .....	63
B.	APPROACH .....	63



C.	RESULTS .....	66
1.	Effect of Sample Thickness .....	66
2.	Radial Stresses at the Interface .....	68
3.	Creep strain distribution during Pushout Creep Testing .....	68
VI.	MODEL FOR DIFFUSION CONTROLLED INTERFACIAL CREEP .....	73
A.	BACKGROUND .....	73
B.	PURPOSE .....	74
C.	THE MODEL .....	75
D.	RESULTS .....	82
1.	Threshold Stress Determination .....	82
2.	Estimation of $h$ and $\lambda$ .....	84
VII.	CONCLUSIONS .....	87
	LIST OF REFERENCES .....	91
	INITIAL DISTRIBUTION LIST .....	95

## ACKNOWLEDGEMENTS

The author gratefully to acknowledges the financial support of this research by the National Science Foundation under Contract # DMR 9423668, with Dr. Bruce A. MacDonald as the program monitor.

I also wish to thank Prof. Indranath Dutta for his persistence, and guidance throughout the course of this thesis work. I am also indebted to Prof. Sarath K. Menon, Dr. R. Nagarajan and R. Hashimoto for the contribution of their time and many useful insights.

Finally, I would like to thank my family and friends for all of their support and understanding. Special appreciation is extended to my wife Camille for her invaluable support.



## I. INTRODUCTION

The automotive and aerospace industries have increasingly focussed their attention on the potential performance gains which will be generated by the use of metal-matrix composites (MMCs) in critical engine and structural components. The low density, high strength, and superior high temperature properties of MMCs are just a few of the attributes attracting developers to this class of materials. For example, Toyota Motor Company has used metal-matrix composites in diesel engine pistons [Ref. 1]. Honda has developed and tested entire engine cylinder blocks composed of aluminum based MMCs [Ref. 2]. The future of turbine engine components is directed toward the incorporation of Titanium or Aluminum matrix composites due to their increased strength, low density and improved high temperature performance [Ref. 3]. Other applications for MMCs in the aerospace/automotive arenas include those in electronics packaging, where the tailorable coefficient of thermal expansion and thermal conductivity of MMCs are utilized advantageously.

The elevated temperature performance characteristics of metal-matrix composites is a key factor which design engineers wish to exploit in future applications. Interest in utilizing metal matrix composites under conditions of high homologous temperature ( $T/T_m$ ) has accentuated the need to understand and accurately predict the time dependent deformation behavior at elevated temperature (i.e., creep response) of this class of materials. A typical metal matrix composite derives its higher strength and improved creep resistance from the ceramic or metallic reinforcements included within the matrix. The reinforcement material can take the form of either dispersed particulates, whiskers, or continuous fibers. However, of all possible reinforcement geometries, introduction of

continuous ceramic or refractory metal fibers into a metallic matrix results in the most significant improvements in creep characteristics.

A metal matrix composite combines the distinct thermo-mechanical properties of the two constituent phases into one body. However, a simple continuum mechanics approach to modeling/prediction of the composite properties is often not adequate if it is based on a uniform stress distribution in each phase and the assumption of isostrain conditions between the fiber and matrix phases. In particular, the latter (i.e., isostrain condition) is often violated during deformation of the composite, leading to the inability of existing approaches to render phenomenologically accurate predictions, which have not been experimentally verified. When placed under load, the inhomogeneity of the composite usually results in a complex variation in active deformation mechanisms, which is a function of both time and position in the composite. Also, several studies have shown that the mechanical properties of composite materials are strongly dependent on the strength and deformation properties of the matrix-reinforcement interface. As a result, fundamental knowledge of the time-dependent deformation mechanisms operating at the interface is a vital requirement in order to correctly predict the creep response of a composite material. Thus, in order to accurately predict the creep behavior of a metal matrix composite it is necessary to understand: (1) the creep response of the individual constituents of the composite, (2) the effect of the complex stress state that exists in a nonhomogeneous deforming body, (3) the interaction between creep and internal residual stresses, and, (4) the role of local stress relaxation mechanisms such as interfacial sliding.

Currently available models for creep in metal matrix composites have used various techniques to account for the possible effect of localized interface deformation or sliding. These models either represent the interface as undergoing frictional sliding [Ref 4.] , or as a

highly dislocated region of the matrix undergoing power law creep with a high stress exponent [Refs 5,6]. A third type of model allows for diffusional accommodation at the interface, and has been applied to discontinuously reinforced composites [Refs. 7,8,9]. However, all of these approaches involve experiments on a complete composite system, followed by the adjustment of some empirical parameter to fit the model to the experimental result, and thence obtaining the "interface" properties. While good agreement between model and experiment has been shown, there is as yet no direct experimental evidence which *isolates and measures the interfacial deformation characteristics*. As a result, no clear phenomenologically based model for interfacial deformation, verifiable by experimental evidence, is available to date. Therefore, in an effort to gain needed mechanistic insight, this study uses a unique experimental approach involving creep testing the *interface* of a model metal-matrix composite. This information is critical in order to develop a kinetics based model capable of describing the longitudinal creep of a continuously reinforced composites under *non-isostrain* conditions.



## II. BACKGROUND

### A. SOME OBSERVATIONS ON COMPOSITE CREEP

A fundamental understanding of the nature of creep in a continuously reinforced metal matrix composite can be obtained through the consideration of the basic composite system shown in Figure 1. In Figure 1 the continuously reinforced composite is placed under a simple uniaxial tensile load. In this system, the fibers are restricted to elastic deformation and the matrix is elasto-plastic and capable of stress relaxation by creep. By assuming an isostrain condition throughout the composite it is possible to utilize the rule of mixtures to model the nature of the evolving stress state in the composite in response to the applied load. Using the rule of mixtures the overall stress in the composite  $\sigma_c$  can be determined from the following equation:

$$\sigma_c = \sigma_f V_f + \sigma_m V_m \quad (1)$$

where  $V_f$  and  $V_m$  are the volume fractions of the fiber and matrix respectively and  $\sigma_f$  and  $\sigma_m$  are the corresponding stresses. For constant applied stress conditions, the derivative of equation (1) with respect to time yields:

$$V_f \frac{d\sigma_f}{dt} + V_m \frac{d\sigma_m}{dt} = 0$$

$$\Rightarrow \frac{d\sigma_f}{dt} = - \frac{V_m}{V_f} \frac{d\sigma_m}{dt}$$

Because the matrix is capable of undergoing stress relaxation due to creep, the time derivative of the matrix stress approaches zero along with that of the fiber. The result is



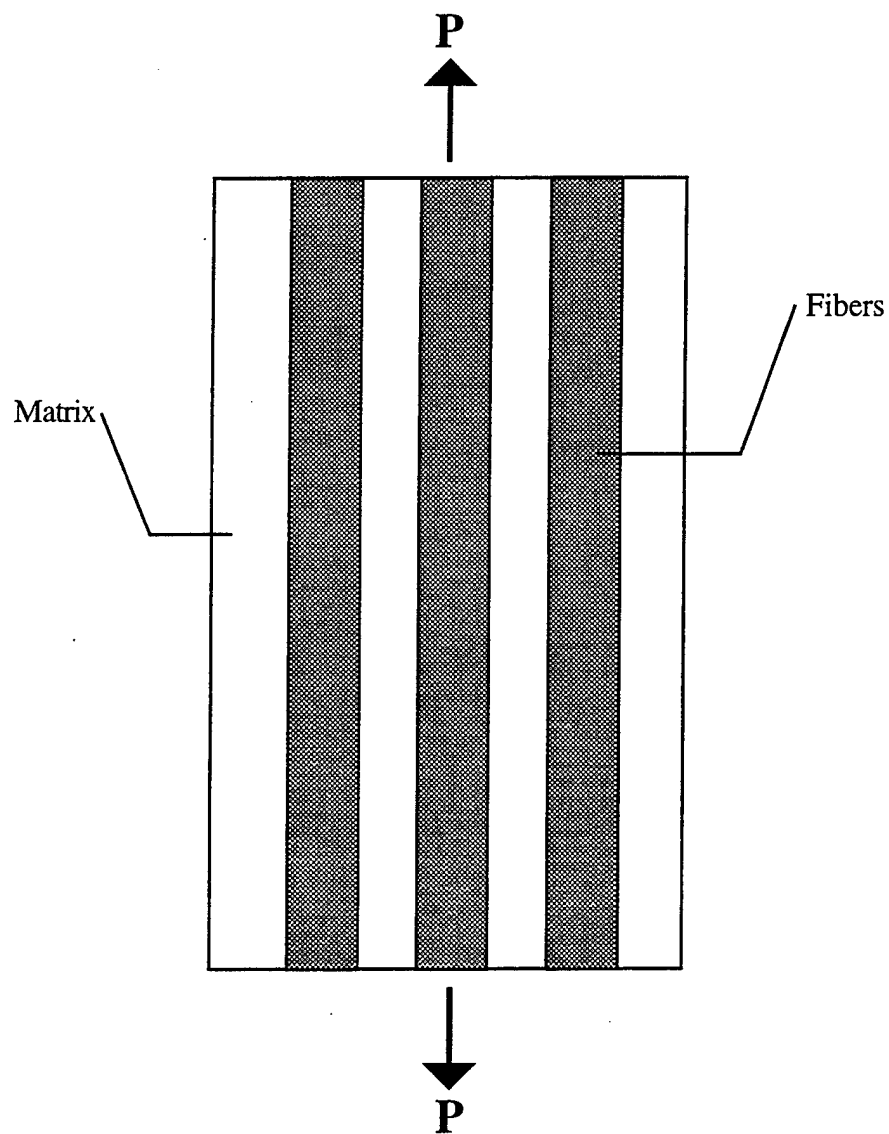


**Figure 1.** Schematic of a continuously reinforced metal matrix composite placed under a tensile load  $P$ . The fibers occupy a volume fraction of the composite  $V_f$ .

that the stress in the matrix is eventually completely relaxed, and the cumulative stress in the fibers equals the composite stress. Consequently, the creep curves of a continuously reinforced composite are expected to be characterized by a transient creep period while the matrix relaxes, followed by an asymptotic approach to a fixed strain value equal to:

$$\epsilon_c = \frac{\sigma_c}{E_f V_f}$$

Thus it is expected that the creep rate of continuously reinforced composites will reach zero after a certain length of time assuming no interface slippage or fiber fracture. This conclusion was reached by McLean [Ref. 10] who studied the creep in a continuously reinforced nickel based superalloy in situ composite with fibers  $\text{Cr}_3\text{C}_2$ . However, McLean's experiments showed that the final stages of creep displayed an increasing strain rate. The increasing strain rate was entirely attributed to fiber fracture, although it is possible that interfacial sliding could also produce a finite steady state creep rate following the initial transient.

Kelly and Tyson [Ref. 11] attempted to perform experiments on silver containing continuous tungsten fibers. Unfortunately, their efforts were frustrated by the premature failure by shear of the solder in the testing grips. The test on discontinuous composites exhibited an increase in the activation energy for creep in Ag-W composites at high temperatures. It was noted that the creep rupture surfaces of the composites tested at elevated temperature showed that no fibers were broken and all pulled out of the matrix, with silver adhering to the sides [Ref. 11]. Matsuura et al. [Ref. 12] were successful in testing an aluminum composite that was reinforced with continuous alumina fibers. Matsuura et al. [Ref. 12] also found evidence of the influence of fiber damage on the initiation of tertiary creep in the continuous composite. As expected, for low stress level without excessive fiber fracture, the creep curve was dominated by the initial primary

transient. Following the primary stage creep, the researchers determined that the specimens were actually undergoing a measurable finite creep rate on the order of  $10^{-9}$  to  $10^{-10}$  s $^{-1}$ . This result is worthy of note because at low stress levels in the absence of fiber fracture and/ or interface failure, any measurable time dependent deformation in a continuously reinforced composite may be attributed to creep at the fiber matrix interface.

Weber et al [Ref. 13] performed creep experiments on  $\gamma$ -TiAl reinforced with continuous alumina fibers. These tests were specifically set up to determine the effect of fiber and interface variables on the longitudinal creep in composites. They applied special coatings to some of the sapphire fibers in order to promote the formation of weak interfaces. The results of these tests were in good agreement with the McLean model [Ref. 10]. A transient creep response was observed and the creep rate diminished with increasing strain (i.e., a transient creep response). In this system, the transient creep response was observed for both conditions, i.e., strong and weak interfaces. Because these tests were all conducted at a single temperature (982 °C), a possible temperature effect on the transient creep response was not considered. A transition temperature effect was not overlooked in the tests conducted by Schwenker and Eylon [Ref. 14] on a Ti-6Al-4V composite reinforced with SCS-6 SiC continuous fibers. At low stresses and temperatures (450 and 538 °C) the predicted transient creep response was noted. However, at the same stress level, but at a higher temperature (650 °C) a small measurable steady state creep rate was observed. According to the acoustic emission data indications of fiber fracture were negligible at the lower stress levels. The mechanism that fully explains the measured creep rate in the absence fiber fracture is the effect of interfacial creep.

Rosler et al. [Ref. 15] performed experiments on TiAl reinforced with Ti $_2$ AlC

platelets. In these creep experiments a transition temperature was identified above which creep strengthening provided by the reinforcement is eliminated. This is attributed to the rapid diffusional flux of matrix atoms from the compressively stressed to the tensile regions of the matrix surrounding the reinforcement via interface diffusion, allowing the matrix to creep as if the elastic inhomogeneity constituted by the platelets did not exist. Dragone and Nix [Ref. 16] conducted studies on the creep properties of a model MMC system composed of a lead matrix reinforced with nickel fibers. Their tests were conducted at 70-87% of the melting temperature of the matrix. While it was determined that the standard form of the Kelly and Street creep model gave good agreement with the trends in the data, Dragone and Nix were only able to obtain an accurate fit to their data after making adjustments to the model which accounted for the effect of a sliding interface. Thus, based on various previously published studies, interfacial strain accommodation appears to play an important role in determining the elevated temperature deformation behavior of composite materials.

## **B. COMPOSITE CREEP MODELS**

Accurately accounting for the deformation properties of the interface region has been an area of difficulty since the earliest efforts to model the creep behavior of metal matrix composites. The initial experimental efforts by Kelly and Tyson [Ref. 11] provided the foundation for the investigation of creep in MMCs. Working with silver reinforced with tungsten fibers, Kelly and Tyson concluded that the rate of creep appears to be governed by the rate of creep in shear of that part of the matrix close to the fiber which is subjected to high shear stress [ Ref. 11]. Following the work of McDanel et al., S. T. Mileiko [Refs. 17,18] chose to ignore the special problem of the interface in his first approach to modeling the creep in composites. Mileiko's analysis is based on considering

the creep of the composite as the summation of the creep of an array of unit shear cells. This cell type of analysis continues to provide useful insight into the properties of composite materials. Mileiko's model is a stress based analytical model which assumes a uniform stress distribution and an isostrain condition between the fiber and matrix. According to this model, as creep progresses within the composite the simple shear cells deform in such a way that there is a free surface created within the composite matrix. Thus, the creep rate is controlled by the movement of these free surfaces or holes in the matrix. Using this approach, Mileiko is able to show reasonable agreement between his model and the results obtained by Kelly and Tyson. Although Mileiko's model of creep by the creation of holes results in a good simplified solution, it fails the test of conceptual accuracy, since it is well established that creep can occur in a continuously reinforced material without the formation of voids or free surfaces. McLean's [Ref. 19] energy dissipation approach to the composite creep problem allowed him to avoid the issue of the complicated internal stress state, although his analysis ignored the role of the interface, and assumed a perfect bond with no sliding at the interface. McLean's analysis resulted in an analytical form which suggests amplification of the internal shear strain occurs between adjacent shear cells in order to satisfy compatibility conditions, relative to the unreinforced matrix. De Silva's model [Ref. 20] for creep in composites is based on: a rule of mixtures form of the composite stress and a perfect interface creating an isostrain condition between the matrix and fiber. De Silva's model, like those discussed above, was generated in order to analyze the creep response of discontinuous aligned fiber reinforced MMCs. De Silva points out that as the matrix stress relaxes due to creep, load is transferred to the fibers via the action of shear stresses. Because the fibers in this model are also able to creep, one condition for the steady state creep is reached when the creep rate in the fibers matches that of the matrix. However, de Silva mentions another steady state condition that fits his model. He has determined that below some critical fiber aspect ratio there is a limit on the

shear stresses that can be generated. As a result, the matrix strain rate no longer equals the fiber strain rate and steady state is achieved by allowing the matrix to creep or slide past the fibers. Although the latter steady state mechanism violated de Silva's perfect bond and strain compatibility assumption, no further explanation was offered with regard to the nature of the interfacial sliding.

The perfect bond assumption (i.e. rigid interface) is not the cornerstone of all composite creep models. In 1972, Kelly and Street [Ref. 4] were the first to incorporate the possibility of deformation or sliding at the interface in composite materials. Their shear lag analysis of the composite creep problem allowed them to incorporate a sliding parameter  $\eta$ . The sliding parameter was a proportionality constant relating the velocity difference between points in the fiber and matrix to the sliding velocity. According to Kelly and Street's model, the rate of sliding along the interface is proportional to the applied shear stress raised to the power,  $m$ . Although the interface was assumed to follow a power-law stress dependence, no clear mechanism was identified to explain the nature of the interfacial sliding. Indeed, the specific value of the stress exponent,  $m$ , was not established, and values of  $m$  ranging from 1 to 14 were considered in their analysis. Further, this form of sliding is linked to the stress dependence of creep in the matrix and does not allow for the possibility of a separate time dependent deformation mechanism operating at the interface. A time dependent mechanism in the interfacial region was proposed by Bullock et al. [Ref. 21] in order to account for the apparent sensitivity of unidirectionally grown eutectic composites to the scale of the microstructure. In their analytical model, the accumulation of dislocations near the fiber was assumed to create a back stress at the interface. The back stress across this region was assumed to have a uniform distribution along the fiber axis and the "interface" was incorporated into the model as a distinct boundary zone

surrounding the fiber with its own independent creep properties. The effect of the boundary layer resulted in better agreement with experimentally observed creep rates. However, there was no direct experimental evidence or mechanistic model offered in order to establish the exact nature of the stress dependence and deformation kinetics of the boundary layer. Goto and McLean [Refs. 5,6] also incorporated the concept of an independently creeping boundary layer in their model of creep in fiber reinforced metal matrix composites. In this model, the interface is regarded as a separate phase of thickness  $\delta$ . Similarly to Bullock et al. [Ref. 21], Goto and McLean assumed an isostrain condition across the composite. As a result, they were able to account for the interface deformation by assigning a unique stress dependence to the matrix boundary layer. However, due to the limited studies performed on continuously reinforced composites at that time, they were unable to rigorously compare their model with experimental results. Such a comparison would have proved useful in order to confirm and explain the possible deformation kinetics of the interface.

In an effort to explain the possible interface deformation kinetics, recent studies have focused on generating creep models which specifically take into account the effects of some form of time dependent interfacial sliding mechanism. Rosler et al. [Ref. 7] have analyzed the effect of diffusional relaxation on creep strength in composite materials. This study shows that the creep strength of reinforced composites may actually be eliminated due to the effect of diffusional flow at the interface. The diffusional flow or sliding of the interface effectively removes the interface tractions which normally act as a constraint on matrix deformation. Based on their analysis, Rosler et al. were able to develop a constitutive equation for overall creep rate which was dependent on the rate of diffusional flow along the interface. From this creep law, Rosler et al. were able to determine both a

critical aspect ratio below which creep strength is lost and a critical transition temperature above which creep strength is eliminated by rapid interface diffusion. The removal of the deformation constraint on the matrix has been analyzed by Kim and McMeeking [Ref. 8]. According to their theory, composite creep strength is equivalently impaired if the interface is either characterized as an interphase layer with minimal viscous drag or as an interface along which rapid diffusion occurs. Thus, they have identified two independent interfacial creep mechanisms in order to explain any possible stress and temperature variation in the creep strength of discontinuously reinforced composites. In their model, the two separate mechanisms constituted: (1) a Newtonian viscous slip at the interface, driven by the interfacial shear stress, and (2) a diffusive flux (i.e., diffusional creep) driven by the normal (radial) stress acting on the interface. Nimmagada and Sofronis [Ref. 9] adopted a similar approach to model the interface deformation and reached similar conclusions. However, they are at variance with Kim and McMeeking with regard to the actual magnitude of the effects of slip and diffusion on creep strength. Nimmagada and Sofronis conducted unit cell analysis and finite element methods to accurately solve for the deformations in the composite and the effect of interface slip and diffusion. Since there is currently no experimental data for interfacial creep by which the two models (i.e., interfacial slip and diffusional flow) can be evaluated and validated, the general trend of creep strength degradation is mainly of qualitative significance. Also, the effect of the reduction in residual matrix stress at elevated temperatures is not considered. The hydrostatic stress state in the composite is evaluated as a function of position but its temperature dependence is not addressed. These two mechanism, viscous drag and diffusional flow, both have the same linear stress dependence and the same direction of flow. Therefore, it is reasonable to consider that there may be one single interface creep law that combines the effects of both normal and shear stresses at the interface.



### C. THE CASE FOR STUDYING INTERFACE CREEP

Independent deformation of the composite interface during creep would constitute a violation of the isostrain condition that is an inherent assumption in most continuum mechanics based creep models. However, experimental evidence exists which would suggest that the isostrain condition between the matrix and fiber is not always maintained during creep [Refs. 22,23]. Also, several metal matrix composite systems have displayed a marked degradation in creep strength at elevated temperatures [Refs. 15,16]. Several studies involving both thermal cycling and creep of metal matrix composites have displayed characteristics that are best explained by interfacial creep mechanisms. Further, the continuous fiber reinforced extremities of specimens which have undergone uniaxial longitudinal tensile creep have been frequently observed to have the matrix extruded beyond the fiber ends, clearly suggesting the breakdown of the isostrain condition and the existence of interfacial sliding in the absence of fracture [Ref. 24]. A schematic representation of this phenomenon is shown in Figure 2.

The most dramatic evidence of an independent interface deformation mechanism is displayed in the results of thermal cycling experiments conducted on continuously reinforced metal matrix composites. Due to the differences in the coefficients of thermal expansion between the matrix and the fiber it is possible to generate high levels of internal stress in the composite by controlled periodic variation in temperature. Dutta et al. [Ref. 22] conducted thermal cycling experiments on aluminum reinforced with graphite fibers. In Figure 3 the specimen was slowly cycled between 298-813K at a heat up rate of 0.89 K/min. Near the edge of the fiber tow it is clearly evident that the matrix has crept out above the fiber to relieve the thermally imposed tensile stress. The sharp step between the top of the graphite fiber and the crept matrix shows that the condition of isostrain between

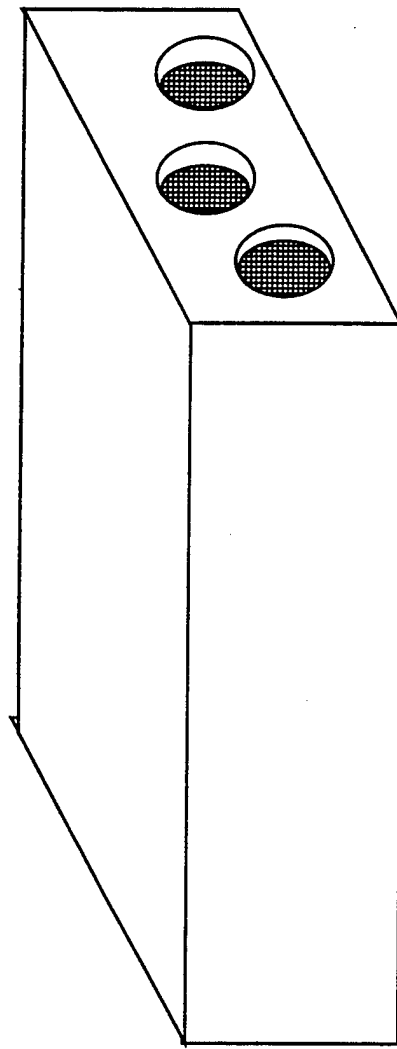


**Figure.2** Schematic of the extremity of a crept continuous fiber reinforced SCS-6-Ti MMC, showing that the matrix has been extruded past the fibers, with a clear discontinuity at the interface, suggesting the existence of interfacial sliding [Ref. 24].

the matrix and the fiber has been violated. This strain incompatibility is significant because the matrix deformation has evidently been controlled by the rate of deformation at the interface and there is no indication that interfacial fracture has occurred. If fracture had occurred in either of these specimens, the matrix and fiber could have relieved the internal stress via a non-time dependent deformation resulting in the matrix (which was initially in residual tension) collapsing below the fiber ends and the fibers (initially in residual compression) would relax by protruding above the matrix. For example, the appearance of a specimen of graphite reinforced aluminum which was cycled between 298K and 318K at a rate of 20K/min is shown in Figure 4 [Ref 25]. Yoda et al. [Ref. 23] performed thermal cycling experiments on a copper composite reinforced with tungsten fibers. Figure 5 shows the microstructure at the end of a specimen that was subjected to 4950 cycles between 673 and 1073K. From Figure 5 it is evident that the matrix has repeatedly crept above the tops of the fibers until the total displacement is nearly one millimeter. Such strain incompatibility across the interface in the absence of fracture must be accounted for with some type of time dependent interfacial mechanism such that the matrix and fibers can display different longitudinal strains while still being linked. Therefore, the determination of the mechanism and kinetics of that interface deformation constitutes the focus of the present thesis.



**Figure 3.** SEM micrograph showing the effect of slow thermal cycling on an aluminum composite reinforced with graphite fibers. The specimen was slowly cycled between 298-813K at a rate of 0.89 K/min. Notice that the matrix has clearly crept and is protruding above the top of the fiber [Ref. 22].

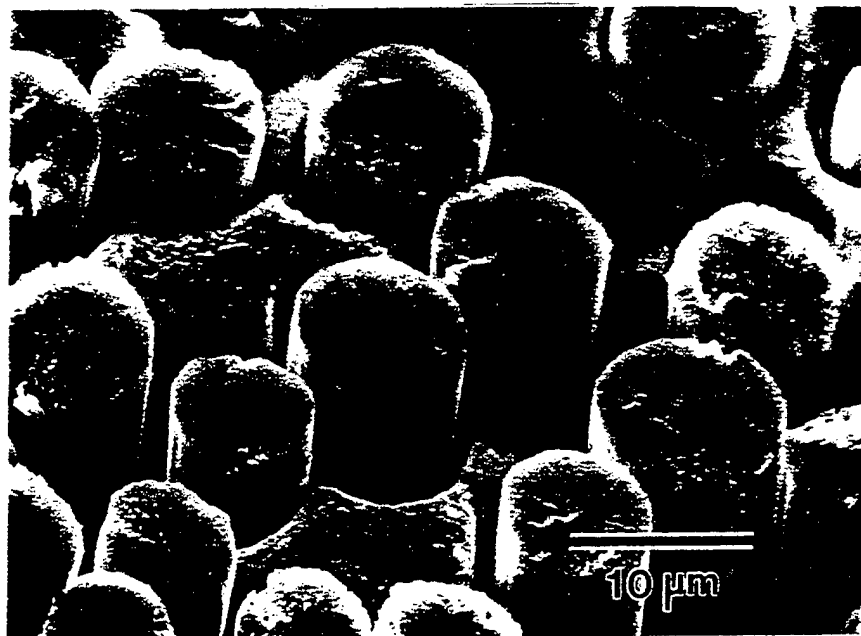


**Figure 4.** SEM micrograph showing the effect of rapid thermal cycling on an aluminum MMC reinforced with graphite fibers. The specimen was cycled between 298K and 318K at a rate of 20K/min. There is clear evidence of interface fracture. The matrix has relieved itself of the tensile residual stress and has collapsed inward, while the fibers which were formerly under compression are protruding out above the matrix.[Ref 25].



**Figure 5.** SEM micrograph of a copper MMC reinforced with tungsten fibers. The image shows the effect of repeated thermal cycling, the specimen was subjected to 4950 cycles between 673 and 1073K. This specimen offers dramatic evidence of the phenomenon of interface sliding. Without any indication of interface fracture, the matrix has extruded above the top of the fiber [Ref 23].



### III. OBJECTIVES

Based on the previous discussion, it is apparent that the accurate incorporation of interface effects on creep in metal matrix composites is contingent on the direct experimental determination of the deformation kinetics. Therefore, one of the objectives of this study is to identify an experimental approach that is capable of providing the necessary data regarding interface deformation without being influenced by the other mechanisms in the composite. The experimental technique utilized accomplishes this goal by isolating the composite interface and precisely measuring the creep characteristics of the interface. The approach chosen in this study constitutes a utilization of a fiber-pushout apparatus to apply a constant force on the fiber of a model single fiber composite, so that the interface can creep under the applied shear stress.

The Finite Element Method (FEM) was utilized to check the conceptual validity of the test approach for one of the model systems, and to provide insight into the design of the sample and test rig. FEM was also utilized to estimate the residual radial stresses present in the model composite system following cooling from an elevated to ambient temperature.

Based on the experimental results, and the FEM analysis, an analytical model is advanced to incorporate the effect of radial residual stresses on the creep of the fiber-matrix interface. The model yields an explicit constitutive law which describes the stress, temperature, and matrix dependence of interfacial creep.





## IV. EXPERIMENTAL

### A. COMPOSITE SYSTEMS

This study analyzes the creep characteristics of the interface in two model metal matrix composite systems. Lead (99.99 % purity) is chosen as the matrix material because its low melting temperature (601 K) allows for the measurement of significant creep rates at near-ambient temperatures. Also the creep properties of pure lead are well documented and there is a wealth of knowledge available for comparison [Refs. 21,22]. The two composite systems studied are lead reinforced with a nickel (Pb-Ni) fiber and lead reinforced with a fused quartz fiber (Pb-Qtz). The model systems were chosen such that the fiber and matrix materials have good wetting characteristics and adhere well with each other. Lead and quartz do not have any solubility in each other, and therefore, the Pb-Qtz system represents the case of a sharp interface. The lead-nickel system is representative of a MMC with a diffuse interface. This is evident from the phase diagram shown in Figure 6 [Ref. 26]. There is a eutectic at 99.87 wt% lead, with practically no solubility of nickel in lead. This results in a nickel-lead interface as shown schematically in Figure 7. Clearly, there is a compositional gradient across the interface, suggesting that the interface may be considered as "diffuse". The relevant thermal and mechanical properties of the constituent materials are delineated in Table 1.

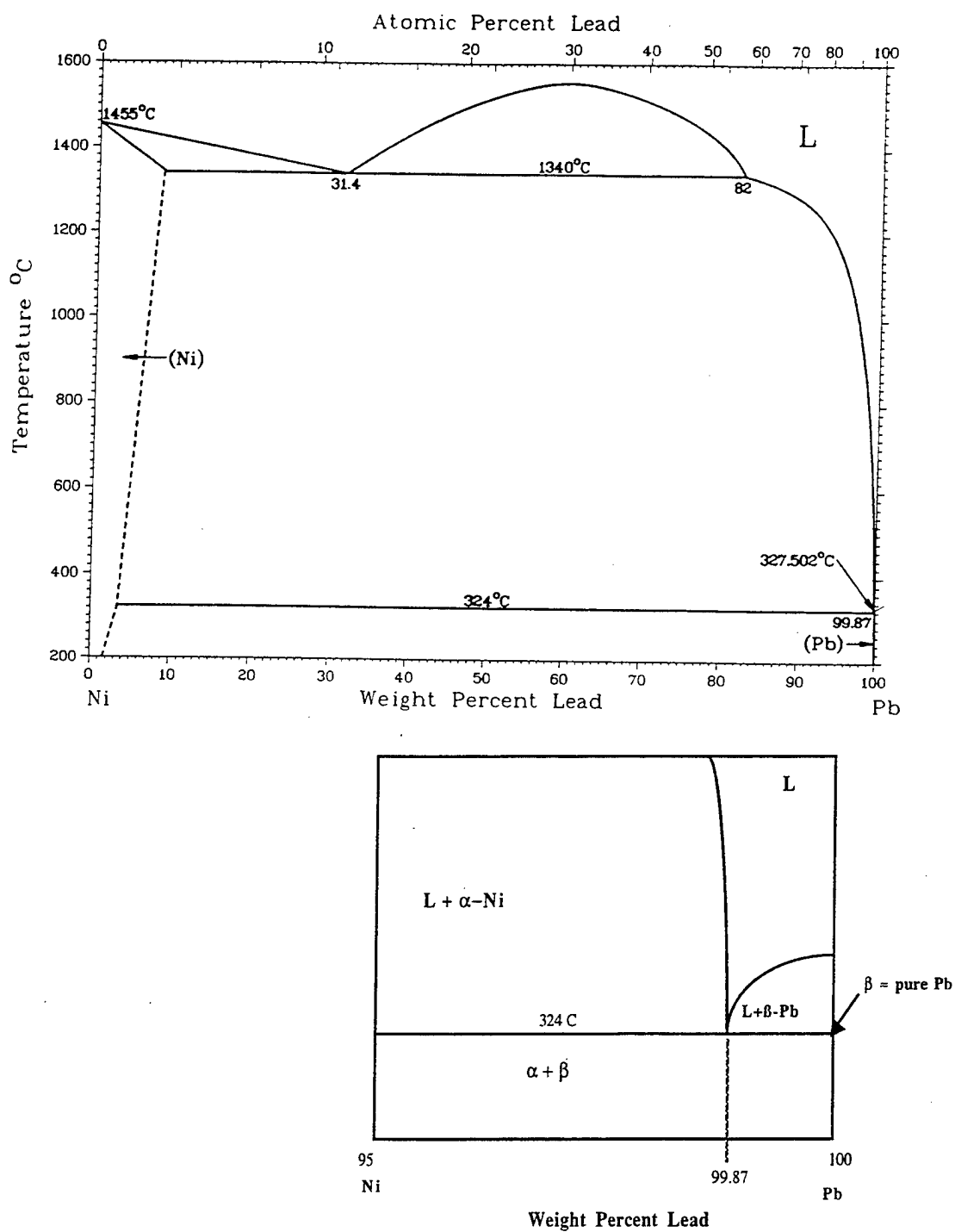


**Figure 6.** Phase diagram of the lead-nickel system. The blow-up shows the region relevant to the interface of the lead-nickel SFC system. Interface region shows solubility which leads to a diffuse interface [Ref. 26].

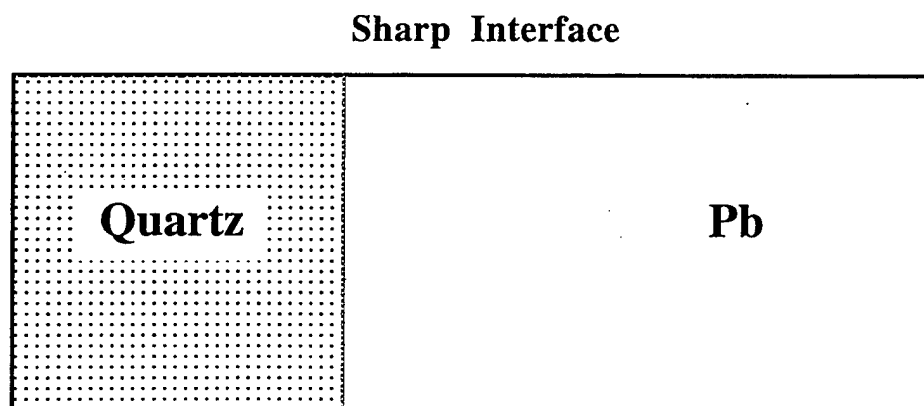
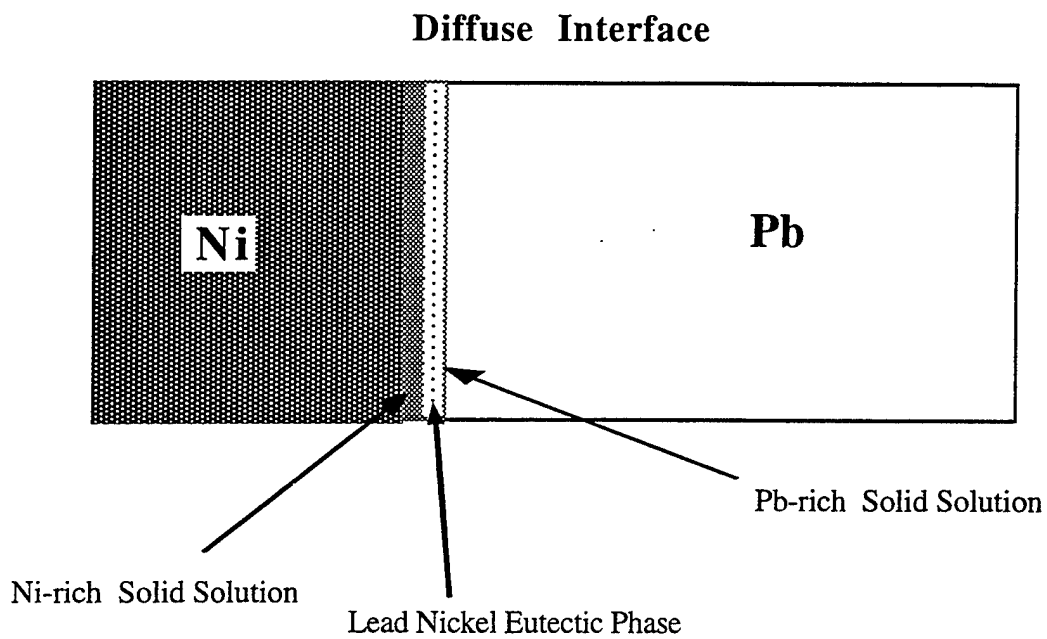


**Figure 7.** Schematic representation of the interface regions in the two types of fiber-matrix interfaces (diffuse and sharp) in the lead-nickel and lead quartz SFC systems.

Property	Lead	Fused Quartz	Nickel
E (GPa) (Youngs Modulus)	16.1	72.74	199.5
$\sigma_y$ (MPa) (Yield Strength)	5.5	1100 (Compressive)	480
$\nu$ (Poisson ration)	0.44	0.16	0.29
$\alpha$ ( $10^{-6}/K$ ) (Coefficient of Thermal Expansion)	29	0.54	13.3
$T_m$ (K) (Melting Point)	601	----	1726

**Table 1. Material Properties**

## B. SINGLE FIBER COMPOSITES

### 1. Fabrication

Lead based single fiber composites were fabricated using a liquid casting technique.

Both the nickel and the quartz fibers had as-received diameter of one millimeter. A three step cleaning process was used to ensure the fiber surfaces were free of contaminants:

- Rinse fibers in 2% dilute solution of NaOH
- Rinse fibers with distilled water
- Final rinse with methanol and hot-air dry

First, lead was melted in a pyrex test tube until a melt temperature of 798 K was reached. Following removal of any surface slag, the Pb melt was poured into a second test tube held inside a furnace. A graphite powder cover was utilized in order to minimize oxidation during melting. The clean fibers were inserted into the melt utilizing an alignment fixture (in order to ensure perfect alignment of the fiber along the test tube axis) and held at 798 K for approximately two minutes. During the holding process and the subsequent cooling, the free surface of the melt was covered with graphite powder (to minimize oxidation) and with a thick layer of alumina (to minimize surface chilling). The model single fiber composites were then furnace cooled to room temperature (298 K) over a period of 4 to 5 hours. The micrograph shown in Figure 8 is an example of the resulting composite microstructure. The edge of the fiber is on the left of the micrograph. The near interface grain size is on the order of 15 - 25  $\mu\text{m}$ . The far-field matrix grain size is somewhat larger, on the order of 25 - 40  $\mu\text{m}$ .

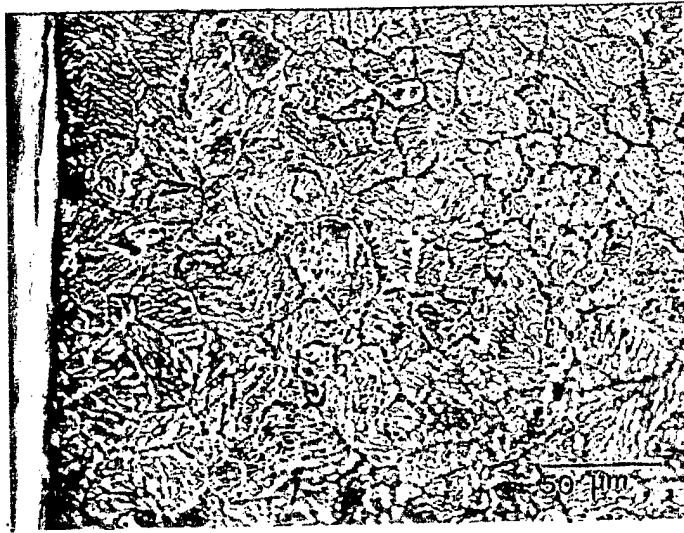


**Figure 8.** Micrograph showing the matrix microstructure in the SFC system. The grain size is on the order of 10-25  $\mu\text{m}$  near the interface and there is a far field grain size on the order of 25-40  $\mu\text{m}$ .

## 2. Specimen Preparation for Pushout/Creep Testing

### a. *Sectioning*

The single fiber composites were cut normal to the fiber axis in 1.5 - 4 millimeter thick sections. The samples were then polished on SiC emery paper coated with paraffin wax. The grit size of the carbide paper was stepped down until the final polishing step performed on 4000 grit paper. The use of paraffin wax was necessary in order to prevent the SiC abrasive particles from becoming embedded in the soft lead matrix.

### b. *Mounting*

The polished specimens were mounted on a four millimeter thick aluminum base plate containing a 1.5 millimeter diameter hole with thermal set mounting wax or colloidal graphite adhesive, such that the one millimeter fiber was aligned exactly over the

hole (see Figure 9). Proper alignment above the hole was verified with a low power stereo-microscope prior to testing.

### **3. Mechanical Testing and Microscopic Examination**

#### **a. *Apparatus***

Figure 10 shows the overall interface testing setup in an MTS 810<sup>TM</sup> servo-hydraulic mechanical testing system. The load cell was set to a full scale range of 448 Newtons. This allowed measurements of the load with an error band of less than  $\pm 0.25$  N. The extensometer used was a high resolution ( $\pm 0.20$   $\mu\text{m}$ ) bridge displacement gauge with a full range from 0-0.51 millimeter. A micrometer controlled X-Y stage was used to ensure the placement of the top of the fiber directly below the center of the flat bottomed indenter. Low thermal conductivity (alumina/mullite) machinable ceramic from Aremco Inc.<sup>TM</sup> was placed in the areas shown in Figure 10 in order to minimize heat loss from the heated elements to the surrounding instrumentation, and thereby affecting the accuracy of the load cell and displacement gauge. The specimen platform and indenter were independently heated by standard Kapton<sup>TM</sup> resistive heating elements from Minco<sup>TM</sup> Products, Inc. The platform and indenter heaters are capable of maintaining constant temperatures up to 125°C with a control band of  $\pm 1$  °C. The geometry of the setup (see Figure 10) is such that the displacement measured by the displacement gauge is equivalent to the fiber-top displacement of the specimen. The arrangement allows for flexibility in the tests that can be performed. For example, in addition to the pushout and creep tests, stress relaxation tests may also be performed using the apparatus. Further, it allows testing a wide range of specimen thicknesses.



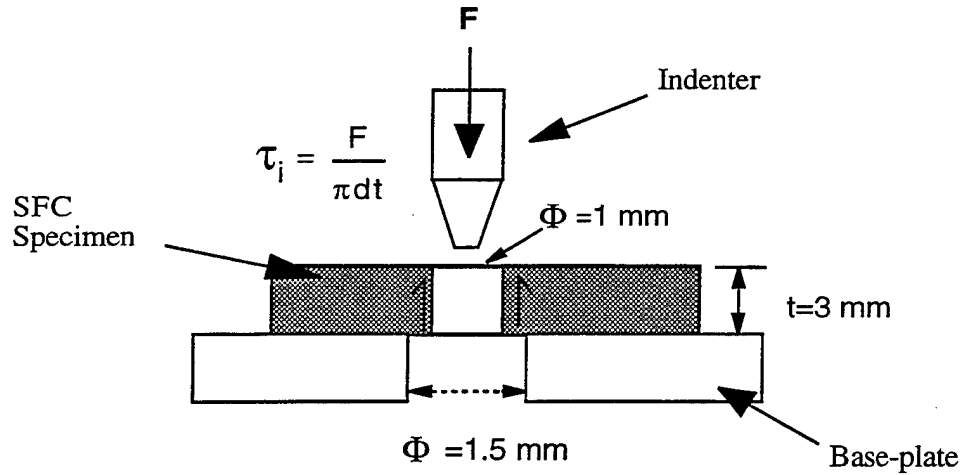


**Figure 9.** Schematic representation of the experimental approach adopted in the pushout/creep test.

### **b. Pushout Testing**

The pushout test was conducted with the servo-hydraulic system, in strain control mode where the hydraulic ram is controlled through feedback from the displacement gauge (see Figure 10). The pushout tests are constant displacement rate tests during which the fiber is pushed out of the matrix and the load required to effect the displacement is continuously monitored. Figure 11 shows a typical pushout curve. The key feature of interest obtained from the pushout curves generated in this study is the linear region prior to peak load, which corresponds to elastic deflection without interface debonding [Ref. 27]. We have designated this load at the onset of debonding as  $P_d$ . The debonding load is then normalized to an average debonding interfacial shear stress  $\tau_d$  which is determined as:

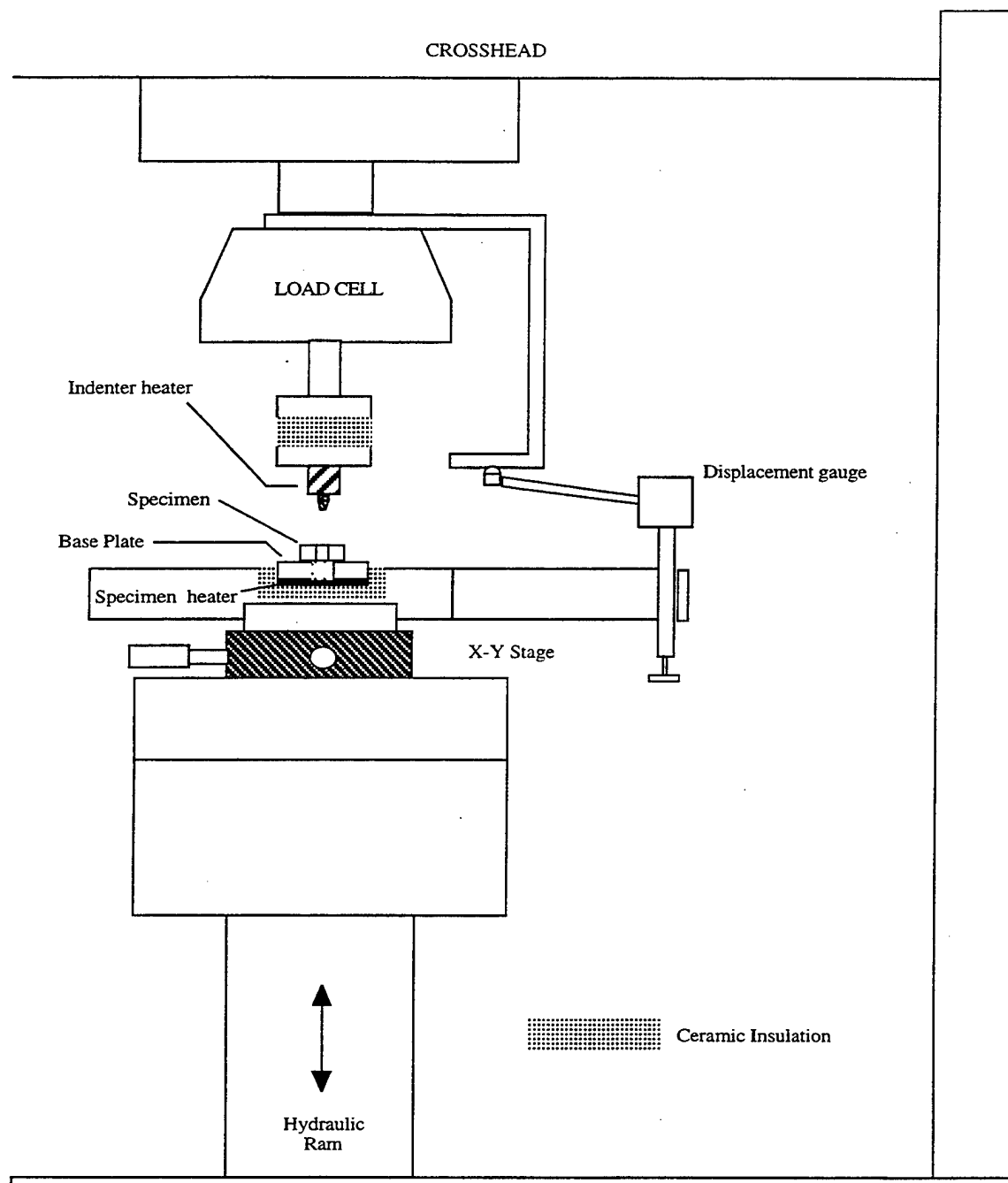


**Figure. 10** Overall schematic diagram of the experimental system used for interface testing. Actual equipment is part of an MTS model 810 servo-hydraulic test system.

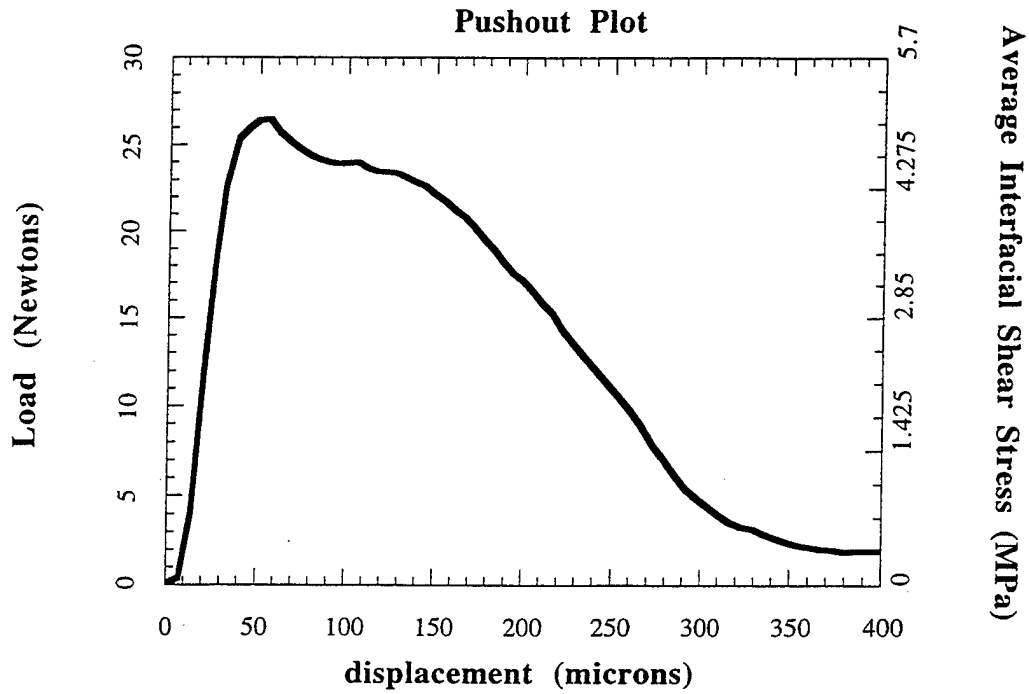


**Figure 11.** Load versus fiber-top displacement curve from a pushout test on the lead-quartz composite system. The point of initial deviation from the linearity corresponds to the onset of fiber-matrix debonding, i.e.  $P_d$ .

$$\tau_d = \frac{P_d}{2\pi r t}$$

where,  $r$ , is the fiber diameter and  $t$ , is the thickness of the specimen.

Elevated temperature pushout tests were performed. Following stabilization and equilibration of the temperatures of the indenter and the SFC sample. This usually took 0.5-1 hour. Several of the pushout specimens were examined in a scanning electron

microscope (SEM) in order to inspect the interface and determine the nature of the fiber-matrix debonding. The SEM images were obtained using a Cambridge™ SEM with a LaB<sub>6</sub> filament operating at 20 kV.

The objective of the pushout tests was to determine the maximum loads that could be applied without causing fracture along the interface. This information was necessary so that the proper loads could be established that would allow for the measurement of creep at the interface without causing fracture.

### ***c. Creep Testing***

Referring to Figures 9 and 10, the interfacial creep tests were conducted under conditions of constant average interfacial shear stress as calculated above. In order to ensure that debonding and fracture did not occur during initial loading, the creep testing was conducted at various stress levels below a maximum stress of  $\tau_d$ . The creep tests were conducted with the MTS unit in load control mode where the output of the load cell controls the position of the hydraulic ram to maintain the applied load at a given setpoint. Displacement measurements from the displacement gauge are continuously monitored during the course of the creep test.

The high temperature creep tests were also conducted in air. Two resistive element heaters were used to conduct high temperature creep testing at various temperatures up to 104 °C. Prior to the initiation of the test, the temperature of the sample is stabilized to match the temperature of the indenter tip. The creep samples were examined in the SEM. These micrographs were collected in order to observe the extent of the deformation which occurred during the creep test.

## **C. DIRECT OBSERVATION OF INTERFACIAL SLIDING**

### **1. Fabrication**

In order to show clear visual evidence of the existence of interfacial sliding, a plate reinforced composite was fabricated in such a way that a free surface containing a longitudinal section of the reinforcement was exposed. A schematic of this model composite is shown in Figure 12. Two composite systems were utilized in this experiment in order to investigate the nature of deformation along the two types of interfaces considered. A tungsten plate was utilized in order to observe the deformation effects along a sharp interface (lead and tungsten have negligible solubility in each other). The lead-nickel composite system was used in this case to determine the effect of a diffuse interface on the nature of the deformation. A liquid casting technique was used to fabricate both model composites.

The alignment fixture used to process the single fiber composites was utilized to maintain the vertical alignment of the plate reinforcement. Lead was then melted in a crucible with a small diameter beaker until a melt temperature of 798 K was attained. The plate reinforcement was lowered into the molten lead, and immediately covered with graphite powder and alumina. The system was held at 798 K for 2 minutes, and then cooled inside the furnace.

### **2. Specimen Preparation**

#### **a. *Sectioning and Polishing***

Following fabrication, the specimens were sectioned through the plate reinforcement using a Beuhler™ high speed diamond saw with a high concentration

diamond blade. The sectioning was performed in order to accomplish three objectives: (1) to ensure that the plate reinforcement was exactly perpendicular to the base of the sample, (2) to guarantee that the base and top of the sample were parallel, and (3) to expose at least one free surface that would provide direct examination of the interface.

The free surface containing the longitudinal section of the plate reinforcement was then polished with SiC emery paper coated with paraffin wax. The grit size of the carbide paper was stepped down until the final polishing step performed on 4000 grit paper. The main focus of the polishing step was to attain a smooth level finish at the exposed matrix reinforcement interface in order to facilitate the proper deposition of a fine carbon grid.

#### **b. *Carbon Grid Deposition***

A high vacuum evaporative carbon coater was used to deposit a grid pattern through a fine 1500 lpi mesh on the sample. The best carbon grid patterns were achieved when the vacuum was less than  $10^{-3}$  torr and the polished surface was two centimeters below the carbon filament. The deposition resulted in a pattern of 19-20  $\mu\text{m}$  carbon film squares aligned across the interface. This same technique has been successfully utilized previously in order to investigate the strains attributable to grain boundary sliding in polycrystalline materials [Ref. 28]

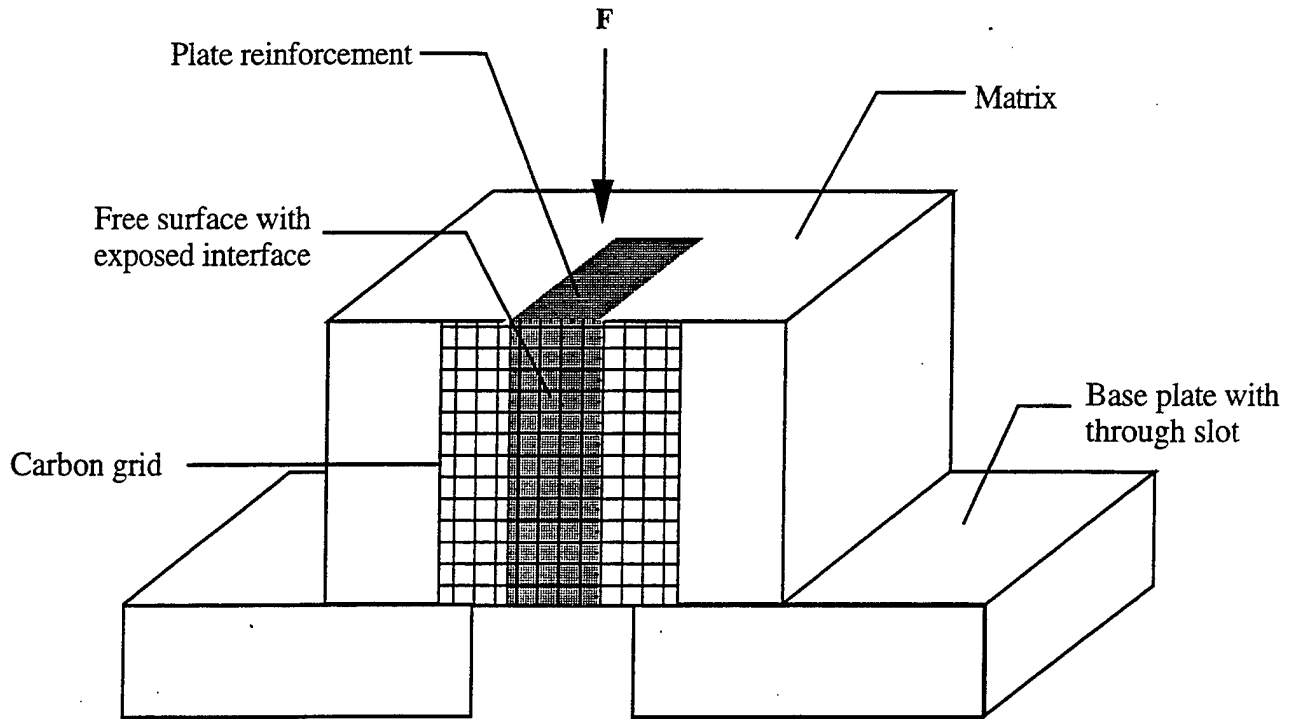


**Figure 12.** Schematic representation of the test approach adopted for the direct observation of interface creep using a plate reinforced MMC with an exposed longitudinal section through the reinforcement. A square carbon grid was deposited across the interface to facilitate observation of interfacial displacement.

### 3. Testing and Microscopic Examination

The matrix-reinforcement interface was viewed in an optical microscope prior to testing. Several images were captured along the interface in order to show the perfect alignment of the carbon grid along the interface prior to testing. The microscopic examination was performed using a Jenaphot™ 2000 optical microscope.

The specimen was then mounted on a four millimeter thick aluminum plate containing a 3 millimeter wide slot using colloidal graphite adhesive. The mounting was

such that the two millimeter wide plate was aligned exactly over the central axis of the slot. Proper alignment above the slot was verified with a stereo-microscope prior to testing. The specimen was then placed in the testing apparatus and a constant load was applied to the top of the plate reinforcement allowing the interface to creep. The load was adjusted upwards as necessary in order to achieve a sufficient creep rate that would yield clearly observable displacements across the interface.

Once the creep tests were completed, the specimen was again examined using an optical microscope. Several images were captured in order to compare the deformed interface with the images taken prior to testing. Figure 12 shows the sample as mounted and the placement of the carbon grid.

#### **D. DATA ACQUISITION**

The data collected during these experiments were acquired using an Apple Macintosh™ computer containing a Strawberry Tree™ data acquisition card. The Strawberry Tree Workbench™ software was utilized to control the data recording and to provide a real time display of the data as it was collected. The raw data was analyzed using the graphing software, Kaliedagraph™.





## IV. EXPERIMENTAL RESULTS

### A. DIRECT OBSERVATION OF INTERFACIAL SLIDING

As discussed in chapter II, there exists experimental evidence that indicates that the strain compatibility between the fiber and matrix may not be maintained during creep in metal matrix composites [Refs. 15,16,22,23]. However, these indications of interfacial sliding have been observed as a result of creep tests on entire composite systems and have not been verified through direct loading of the interface in shear. In order to directly examine the contribution of interface deformation to the overall composite deformation, the experiment introduced in the previous section was performed on the lead matrix composite reinforced with a tungsten plate. Figure 13 shows the vacuum deposited carbon grid pattern as it initially appeared across the interface. In Figure 13, the tungsten reinforcement is on the right, the lead matrix is on the left, and there is a distinct interface evident between the two constituents. It is important to note that prior to testing the grid pattern was in perfect alignment across the interface.

A stress change creep test was performed on the sample using the setup shown in Figure 12. The resulting creep curve is shown in Figure 14. The sample was initially loaded to attain an average interfacial shear stress of 0.05 MPa. This load was maintained for 2.5 hours and then the load was increased to attain an average shear stress level of 0.08 MPa and maintained for another 2.5 hours. As shown in Figure 14, the displacement measured as a function of time during the course of the test reveals that the deformation between the reinforcement and matrix has a distinct time dependent characteristic, suggesting that the interface is undergoing creep.

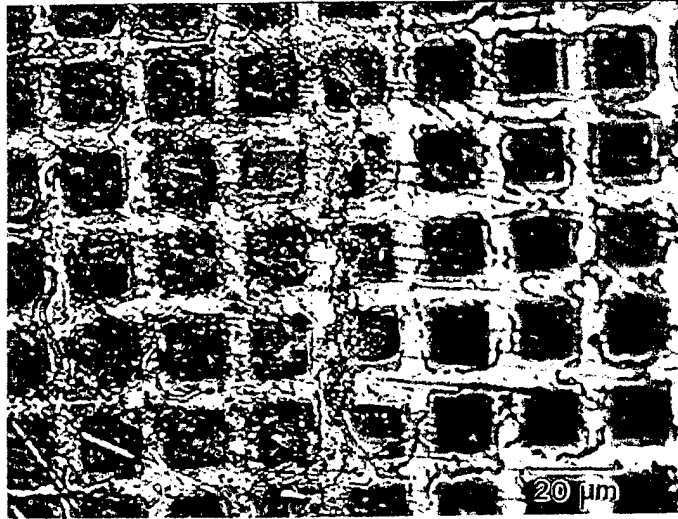


**Figure 13.** Optical micrograph showing the deposited carbon grid pattern across the reinforcement-matrix interface. There is perfect alignment of the grids on both sides of the interface. In the image, the matrix (lead) is on the left and the reinforcement (tungsten) is on the right.

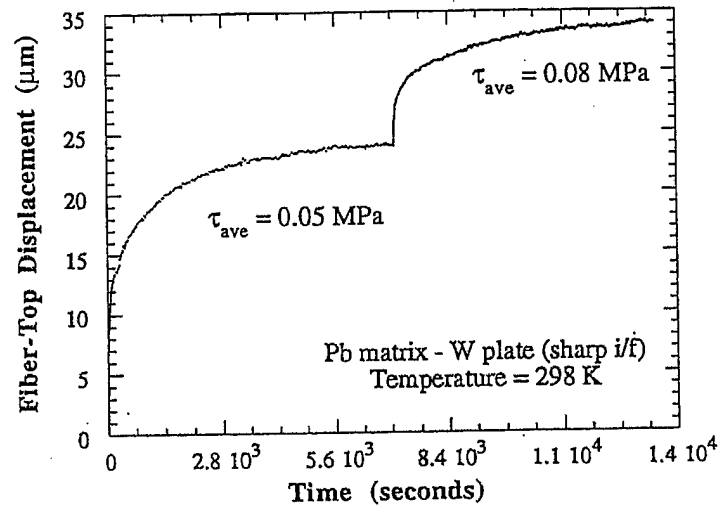


**Figure 14.** Fiber-top displacement vs. time plot obtained during the test to directly observe the effect of interfacial sliding. The distinctive feature of this curve is its clear time dependent characteristic.

After completing the creep test, the sample was again examined in the optical microscope to check for any indication of relative displacement between the reinforcement and matrix. Figure 15 clearly shows that after the creep test, there was a distinct displacement between the reinforcement and the matrix. Upon examining the grid pattern in the matrix, it is evident that the amount of matrix deformation is negligible compared to the definite grid discontinuity at the interface. From these observations it can be determined that the measured deformation is dominated by creep along the interface. No evidence of fracture was observed at the interface.

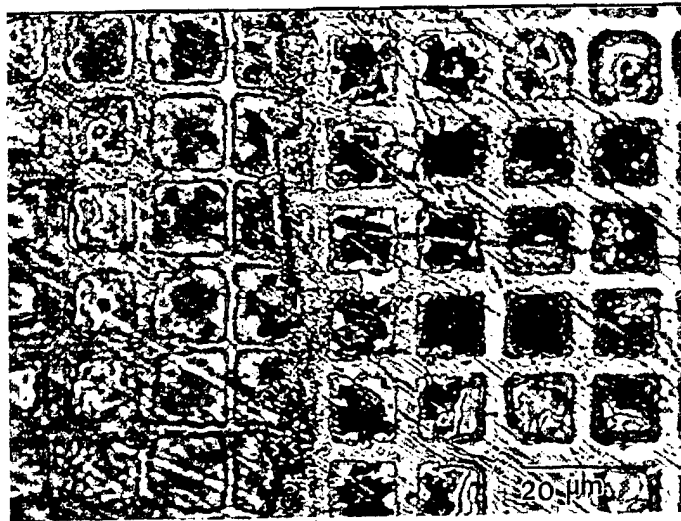


**Figure 15.** Optical micrograph showing the appearance of the deposited grid pattern across the interface following a stress change creep test. The deformation of the grid reveals a negligible matrix component and a sharp discontinuity at the interface. In the image, the matrix (lead) is on the left and the reinforcement (tungsten) is on the right.

The above experiment produces incontrovertible evidence that at least in the stress / temperature regime of the experiment, the interface displays time dependent creep

behavior, with the interfacial creep rate being significantly larger than the creep rate of the adjacent matrix. Thus, clearly, the interface has its own deformation kinetics, separate from the deformation kinetics of the matrix. Now that the existence of interfacial creep has been clearly observed, the following experiments were conducted to gain insight into the kinetics of the creep mechanism.

## **B. PUSHOUT TESTING**

As shown in figure 4, interface fracture is also a mechanism that can be used to explain a violation of strain compatibility between the fiber and matrix. However, the focus of this study is on the determination of deformation mechanisms at the interface without fracture. Therefore, in order to conduct creep experiments in a stress regime such that there is no chance of interface fracture, some basic understanding of the fracture strength of the interface must be obtained. Several studies have shown that the single fiber pushout test can be successfully utilized to determine the shear strength characteristics of the fiber matrix interface [Refs. 27, 29-36].

### **1. Lead-Quartz System Pushout Tests**

The setup for the pushout tests was as shown in Figure 9. Two pushout tests were conducted for the lead-quartz composite system. One test was conducted at room temperature (298 K) while the other test was conducted at the highest expected temperature for creep testing (373 K). Sample thicknesses were 1.7 mm (298 K test) and 2.3 mm (373 K test). The displacement rate for the pushout was set to 40  $\mu\text{m/s}$ . The average interfacial shear stress versus displacement measurements are shown in Figure 16 for both temperatures. As discussed in chapter III, the departure from linearity is associated with the onset of partial debonding along the fiber matrix interface. Figure 16 shows that at

room temperature (298 K) the onset of debonding does not occur until the shear stress reaches a level of  $\approx 4.8$  MPa and complete debonding takes place at 5 MPa. However, the elevated temperature pushout test (373 K) displays a distinct departure from linearity at a stress level of only 1.2 MPa and complete debonding occurs at 3.2 MPa. In both curves, the peak load corresponds to complete interface fracture. The stress measurements following the peak are generated as a result of frictional sliding. Acoustic emission tests

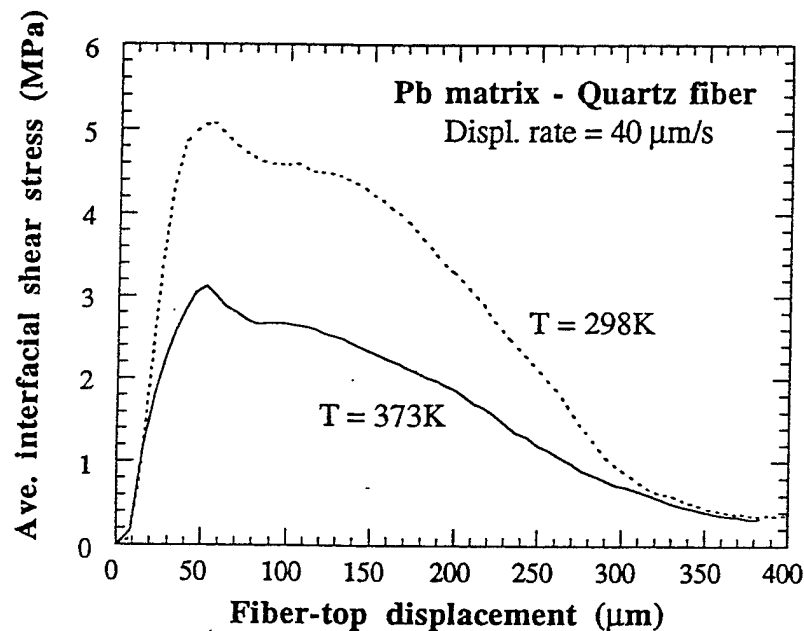


**Figure 16.** Pushout curves for the lead quartz composite system. The interfacial shear strength is noted to decrease as temperature increases.

conducted during the course of the elevated temperature pushout confirm that the peak stress corresponds with a large acoustic signal which is most likely commensurate with complete interface fracture. The subsequent frictional sliding generated negligible levels of acoustic signals. Therefore, it is assumed that the debonding in the lead-quartz system

takes place via a mechanism of unstable fracture.

The pushout samples were examined in the SEM to check for indications of the nature of the debonding. The SEM micrographs shown in Figure 17 reveal the appearance of the top and bottom surface of the sample subjected to elevated temperature pushout testing. The sharp clearance at the interface indicates that debonding is likely to have occurred by initial interfacial fracture at the top, followed by continued downward crack propagation until complete debonding occurred. It is also possible that debonding occurred according to the model suggested by Chandra and Ananth [Ref. 27]. In this model, debonding initiates first from the bottom surface then a following debond occurs on the top surface and propagates downward until the two cracks meet in the middle of the fiber (i.e. both top and bottom debonding occur).

## **2. Lead-Nickel System Pushout Tests**

In Figure 18, the pushout curves for the lead-nickel system show a markedly different appearance than those recorded for the lead-quartz system. The pushout tests were conducted at 313, 343, and 373 K to gauge the effect of increasing temperature on the interface fracture strength. The peak debond load at all three temperatures was significantly higher than that measured in the lead-quartz system. The sample tested at 313 K displayed indications of the onset of debonding at a stress of 6 MPa, while the sample tested at 373 K had a debonding onset at a stress of 4.2 MPa. As expected the sample tested at 343 K exhibited fracture strength properties intermediate to the other temperature extremes. The shape of all three pushout curves are distinctive. The lead-quartz pushout curves were characterized by that sharp debond peak and a sudden stress drop. However, none of the lead-nickel pushout tests exhibit a sharp debond peak. In fact, they are characterized by a

blunted debond peak indicating a gradual, stable interface debonding mechanism initiated from the top of the fiber. This distinctive behavior is also corroborated by acoustic emission data that reveals significant acoustic signals throughout the course of the pushout up to and including the region following the peak load. The diffuse nature of the

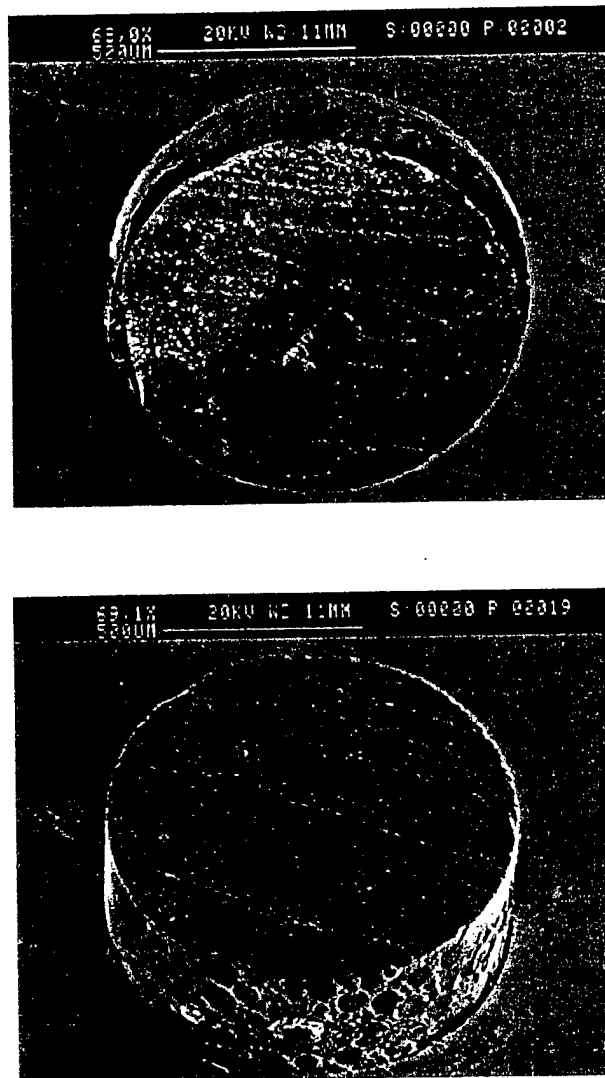


**Figure 17.** SEM micrographs showing the top and bottom faces of a lead-quartz composite that has undergone a single fiber pushout test. This pushout was conducted at a temperature of 373 K. Note the sharp interface edges indicating possible top and bottom debonding.



lead-nickel interface is offered as a possible explanation for the difference in the interface strength characteristics. Also, the normal strength of the lead-nickel metallic bond is expected to be substantially greater than the bonding that exists between a metal and a ceramic such as quartz.

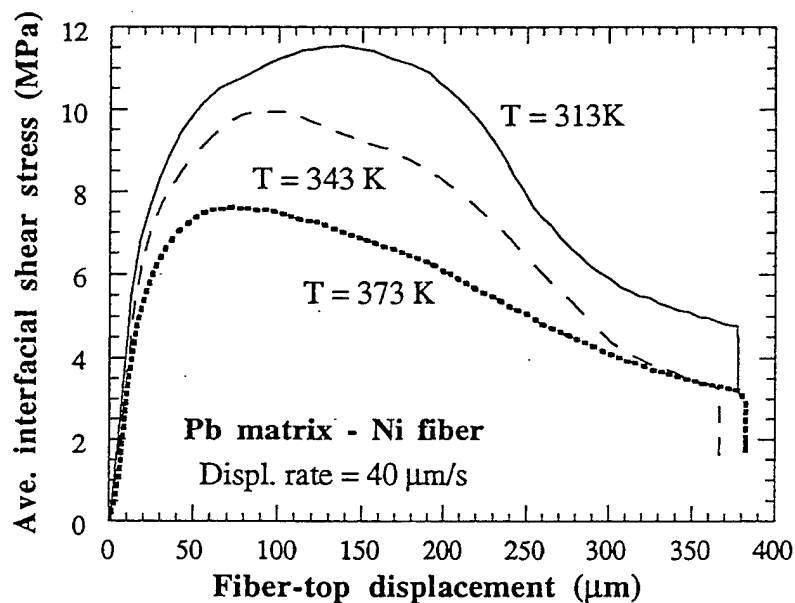


**Figure 18.** Shear stress versus fiber-top displacement curves measured during the pushout tests on lead-nickel single fiber composites. There is a decrease in the interfacial strength at elevated temperatures. The 313 K sample exhibits a 11.8 MPa peak with a debonding onset point at 6 MPa. Note the peak has a more blunted appearance than in the lead-quartz system.

The SEM micrographs in Figure 19 reveal the appearance of the top and bottom

surfaces of the sample subjected to pushout testing at 343 K. The top of the sample has the same characteristics as those shown in the lead-quartz case. The sharp edge at the interface indicates that debonding initiated from the top of the fiber and propagated downward. However, the bottom of the sample reveals some interesting features. On one side, the bottom of the fiber is clearly sticking out and there is a sharp discontinuity at the base of the fiber where the interface has practically fractured. However, on the other side of the fiber, there is a gradual slope where it appears that the matrix/interface has undergone extensive plastic flow and the matrix is still attached to the edge of the fiber. It is important to note that the scale of this interfacial zone appears to be on the order of 50  $\mu\text{m}$  thick. This feature is in no way associated with the hole in the specimen support plate, as the dimensions of that hole place its perimeter outside the frame of the photograph. Thus, the stronger metallic bond, combined with the microstructure of the lead rich eutectic surrounding the fiber, may have contributed to the observed plastic deformation along the interface. Clearly in this case, debonding starts at the top surface of the specimen and progresses downward, and appears to have resulted in pushout in the absence of complete debonding at the bottom face. The incomplete debonding and plastic flow may possibly be attributed to rapid diffusional accommodation at a thin interfacial layer between the fiber and the matrix.

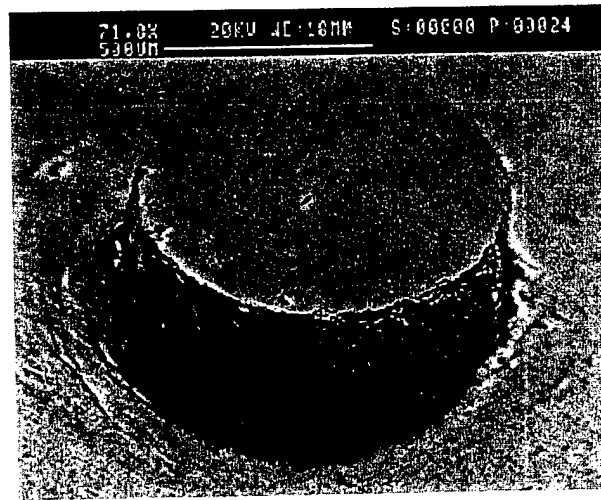
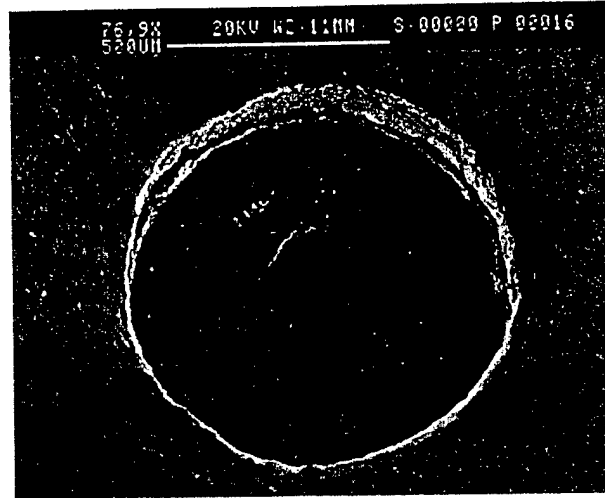


**Figure 19.** SEM micrographs showing the top and bottom surface of a lead-nickel composite system specimen. The specimen has undergone a pushout test. There is indication of top face debonding. Note the left edge of the bottom of the fiber still has a thin ( $\approx 50 \mu\text{m}$ ) interface layer attached to the side.

### 3. Pushout Test Summary

Table 2 summarizes the average interfacial shear stress corresponding to initial debonding obtained from the single fiber pushout tests.

Temperature	Lead-Quartz SFC	Lead-Nickel SFC
298 K	4.8 MPa	--
313 K	--	6 MPa
343 K	--	5 MPa
373 K	1.2 MPa	4.2 MPa

**Table. 2** Summary of the average interfacial shear stress at the onset of debonding for both single fiber composite systems at various temperatures.

### C. CREEP RESPONSE OF THE INTERFACE

With the information obtained from the pushout tests, a series of experiments were performed on both single fiber composite systems using the setup from Figure 9. These tests focussed on determining the temperature and stress dependence of the secondary stage (apparent steady state) of the observed creep response. Thus, the constant creep rate (during the apparent steady state) is used to gain insight into the deformation kinetics of the interface.

Tests were conducted at room temperature (298 K) at various stress levels in order to determine the stress dependence of the mechanism of interfacial creep. Following the

stress dependence tests, creep experiments were performed at the same stress level at various temperatures. Creep mechanisms are expected to obey a temperature dependence according to the Arrhenius equation:

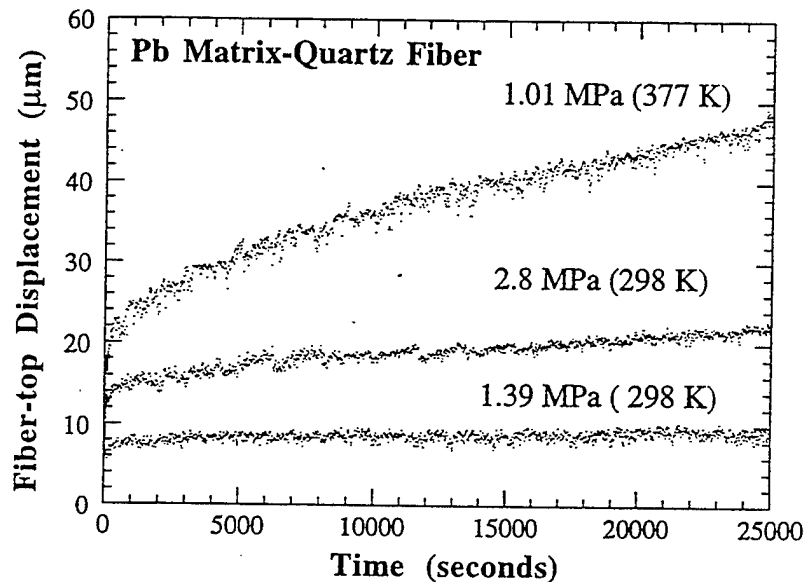
$$\dot{U} \propto \exp\left(-\frac{Q}{RT}\right)$$

where  $\dot{U}$  is the average interfacial displacement rate, as measured by the time-dependent displacement of the fiber top,  $R$  is the universal gas constant,  $T$  is the absolute temperature, and  $Q$  is the activation energy for the operative mechanism of creep. As a consequence of this relationship, creep tests at constant applied average interfacial shear stress and under varying temperature creep conditions can be used to determine the magnitude of the activation energy. This activation energy value can then be compared with the material specific values previously determined, and thus information on the nature of the mechanism may be obtained. Additionally, by plotting  $\dot{U}$  versus  $\tau_{ave}$  (applied average interfacial shear stress), a functional relationship may be obtained between the creep rate and the applied stress.

## 1. Lead-Quartz SFC Creep Response

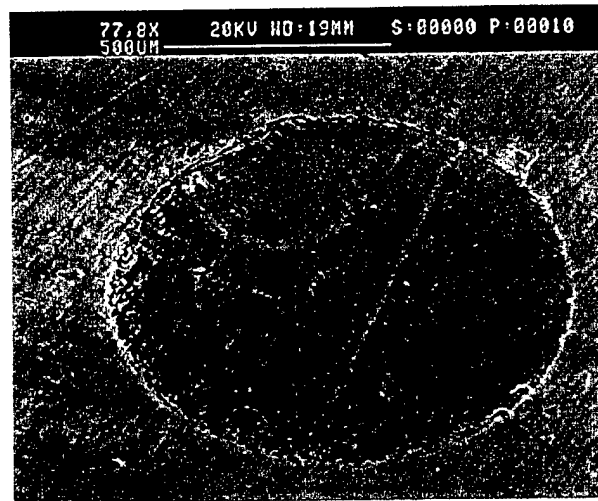
Room temperature interfacial creep experiments ( $\approx 298$  K) were conducted on lead-quartz single fiber composite specimens as stress levels from 1.3 to 3.75 MPa. The nominal sample thicknesses was 3 mm. Elevated temperature creep experiments were conducted at temperatures ranging from 313 K to 377 K. Based on the results of the pushout tests, the elevated temperature creep tests were conducted at a constant stress level of 1.01 MPa, which was determined to be substantially below the average interfacial shear stress level corresponding to debond initiation.

Figure 20 shows three representative fiber-top displacement versus time curves measured during the course of these tests. For the two tests conducted at room temperature there is small but distinct difference between the measured secondary stage creep rate, thereby indicating a low stress dependence. As expected the elevated temperature test exhibits a significantly higher secondary stage creep rate even though it was performed at a lower stress level. The Arrhenius type of temperature dependence (i.e. exponential) is expected to yield dramatic variation in creep rate as a function of temperature.

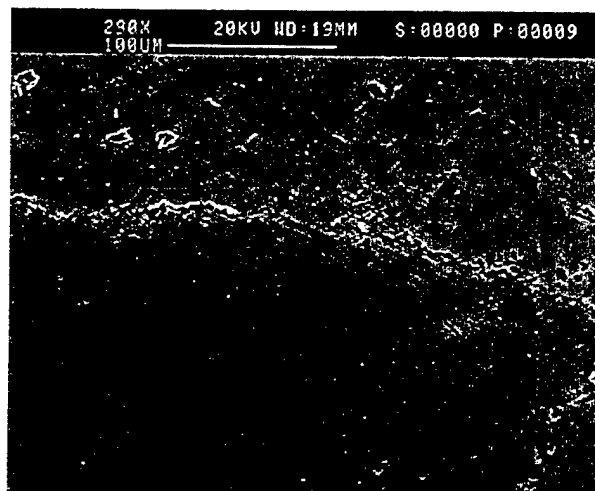


**Figure 20.** Results of interfacial creep experiments performed on lead-quartz single fiber composites. Notice that all curves are characterized by a transient primary stage followed by a secondary stage with a constant creep rate.

After creep testing, some of the specimens were examined in the SEM to determine whether the nature of the creep deformation could be detected via a surface examination. Figures 21( a &b) and 22 are SEM micrographs of the top and bottom faces of a sample which underwent creep at an average interfacial shear stress of 3.25 MPa for 5 hours. Figure 21b shows the edge of the fiber at the top of the sample at a high magnification. Inspection of this image reveals a distinct step near the interface where the fiber has crept downward into the lead matrix. The sharpness of the step, and the apparent absence of a gradual slope in the matrix immediately adjacent to the fiber, suggests that the measured time dependent displacement is attributable directly to interface creep, with negligible contribution of matrix creep. Figure 22 shows the bottom of the sample, and again there is a distinctive edge where the fiber has crept out of the matrix. It is important to note that the sharp discontinuous nature of the displacement, combined with the time dependent displacement curve clearly indicates that creep has occurred and that the deformation is dominated by interfacial sliding.



(a)



(b)

**Figure 21.** SEM micrographs at (a) low magnification and (b) high magnification of the top of a lead-quartz composite interfacial creep specimen. The average interfacial shear stress was 3.25 MPa applied for 5 hours. The the closeup below shows a distinct step at the fiber-matrix interface.



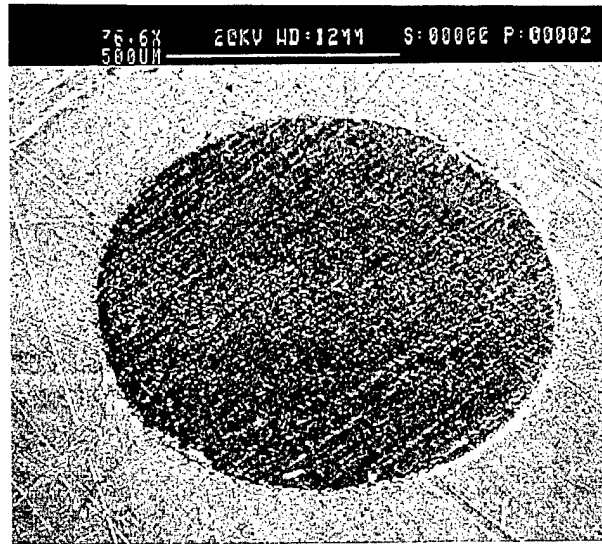


**Figure 22.** SEM micrograph of the bottom face of a lead quartz SFC following creep testing. Notice the sharp edge where the bottom of the fiber is above the bottom face of the sample.

## 2. Lead-Nickel SFC Creep Response

As in the previous section, creep experiments were performed on the lead-nickel single fiber composite system over an array of stresses and temperatures. Room temperature interfacial creep experiments ( $\approx 298$  K) were conducted on lead-nickel single fiber composite specimens as stress levels from 0.6 to 3.9 MPa. Again, the nominal sample thickness was maintained around 3mm. Additionally, experiments were conducted at various temperatures under conditions of a constant applied average interfacial shear stress ( $\tau_{ave}$ ) of 1.5 MPa.

Figure 23 shows three representative examples of the creep curves gathered during these experiments. All three curves are characterized by a transient period of decreasing

creep rate followed by a secondary stage of constant creep rate.

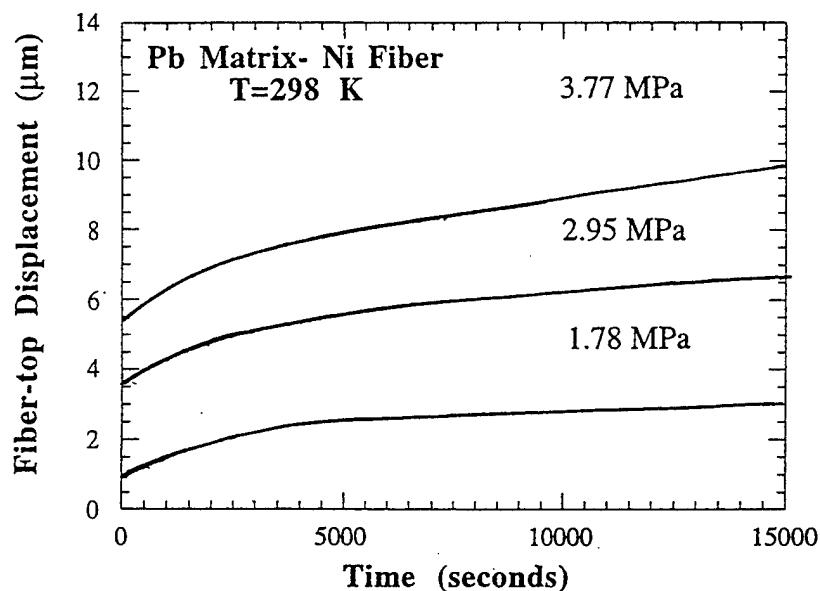
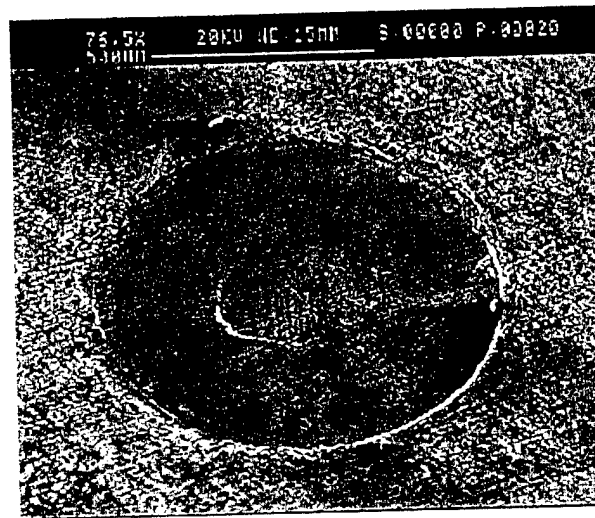
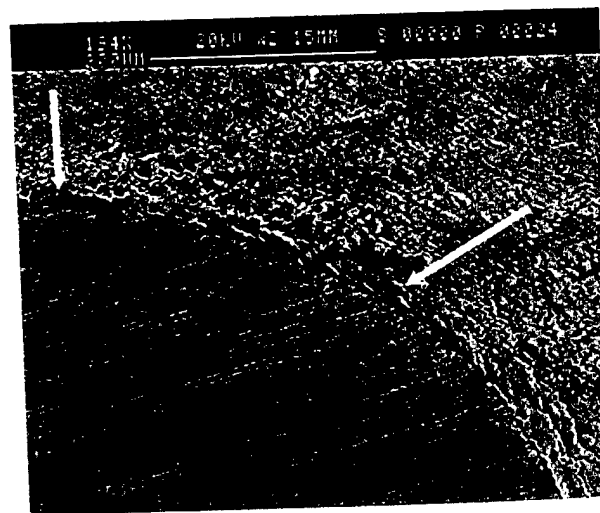


**Figure 23.** Results from interfacial creep experiments performed on lead-nickel SFCs at room temperature (298K). Notice the increase in secondary stage creep rate as the stress level increases.

The SEM micrographs shown in Figures 24 (a and b) and 25 strikingly reveal the nature of the fiber-top displacement. The sample shown was creep tested at an average interfacial shear stress of 3.25 MPa for 12 hours. The length of the creep test was extended in order to obtain a creep deformation that was visually discernible. There is a well-defined step on the top face of the sample in Figure 24. The two arrows in the high magnification view of the top face (Figure 24b) clearly indicate a sharp step at the interface, suggesting that the interface has undergone creep deformation, with little associated creep of the matrix in the vicinity of the fiber. Also, in Figure 25, there is a raised boundary zone around the bottom of the fiber which corresponds with the deformation observed on the top face.



(a)



(b)

**Figure 24.** SEM micrographs of the lead-nickel SFC at (a) low magnification and (b) high magnification showing the effect of an interfacial creep test on the fiber-matrix interface profile. The sample was tested with an applied average interfacial shear stress of 3.25 MPa for 12 hours. Note the well-defined step at the fiber-top matrix interface.



**Figure 25.** SEM micrograph showing the bottom face of a post creep test lead-nickel SFC. The specimen was tested at a stress level of 3.25 MPa for a period of 12 hours. There is a distinct raised boundary zone around the perimeter of the fiber.

#### **D. ANALYSIS OF CREEP RESPONSE**

Despite the assumed microstructural differences between the interfaces of the two composite systems (i.e., sharp and diffuse), the results of the constant temperature creep test reveal strikingly similar linear stress dependence for both systems. Figures 26 and 27 summarize the results of the room temperature tests for the lead-quartz and lead-nickel composite systems, respectively. The measured fiber-top displacement rate during secondary creep ( $\dot{U}$ ) is plotted as a function of the average applied interfacial shear stress ( $\tau_{ave}$ ). In both systems, a linear stress dependence of the interfacial creep rate is observed. Additionally, in both systems, the existence of a threshold stress ( $\tau_0$ ), below which no

measurable interfacial creep occurs, is apparent (Bingham flow). In the lead-quartz system this threshold stress is on the order of 1.4 MPa (Figure 26), whereas for the lead-nickel system the threshold stress is  $\sim 0.7$  MPa (Figure 27).

The linear stress dependence of the interfacial creep rate, as observed in both systems, suggests that interfacial creep is controlled either by diffusional flow, or by Harper-Dorn dislocation creep. Of these, the latter may be eliminated forthwith as a possibility since: (a) experimental evidence strongly suggests that the measured displacements are almost entirely confined to the interface, and have no perceptible contribution from the matrix; and (b) since the matrix grain size near the interface in the experimental system is  $\sim 15 \mu\text{m}$ , which is far too low to cause detectable matrix creep by the Harper-Dorn mechanism.

Therefore, the evidence is strongly in support of an interfacial sliding mechanism accommodated by diffusional flow of matter along the interface, controlled by either matrix or interface diffusion.

Figure 28 summarizes the results on the temperature dependence of creep rate, based on the lead-quartz composite system. By plotting the natural log of the measured creep displacement rate as a function of the reciprocal of the absolute temperature ( $1/T$ ), the resultant plot yields a straight line with a slope of  $-Q/R$ , where  $Q$  is the apparent activation energy of the rate controlling mechanism for interface creep. For the lead-quartz system,  $Q$  was determined to be 51.8 kJ/mol. This is roughly half the activation energy for volume diffusion in lead (109 kJ/mol), and is significantly less than the activation energy for grain boundary diffusion in lead (66 kJ/mol). This suggests that at least in the case of the lead-quartz system, which has a sharp interface (lead and quartz have no mutual solubility), the

interface behaves much like a free surface and the activation energy for creep at the interface is equal to that for surface diffusion. Thus, for sharp interfaces, the rate of interfacial creep is likely to be controlled by the rate of surface diffusion. (The apparent value of  $Q_i$  assumes that  $\tau_0$  is constant, i.e., possible temperature dependency of  $\tau_0$  has not been evaluated).

Based on the experimental results, the phenomenological form of the rate equation for interfacial creep may be written as:

$$\dot{U} = K (\tau - \tau_0) \exp(-Q_i/RT)$$

where  $\tau$  is the applied average interfacial shear stress,  $\tau_0$  is the measured threshold stress,  $Q_i$  is the activation energy for the rate controlling process (interface diffusion),  $R$  is the universal gas constant, and  $T$  is the absolute temperature.

In viewing the general form of the interface sliding equation the main question that must be answered is what constitutes the physical basis for the threshold stress behavior. Models for pure diffusional control of the creep process are unable to explain the existence of a threshold stress for diffusional flow. Diffusional flow with a threshold stress (Bingham flow) has been explained on the basis of the rationale that there needs to be stress-activated generation and absorption of vacancies (e.g., at grain boundaries and interfaces), since grain boundaries / interfaces are not "perfect" sources and sinks for vacancies. Typically, such stress-activated generation / annihilation of vacancies have been associated with complicated interfacial dislocation mechanisms, which are difficult to verify experimentally [Refs. 36-38]. However, the results of these experiments in conjunction with the model developed subsequently (see Chapter VI), indicate another possible origin for the observed threshold stress. The fact that the measured threshold stress is greater in the lead-quartz system is interesting when one considers that the magnitude of the

difference in the coefficient of thermal expansion between the two constituents is also greater in the lead-quartz system. As a result of the higher  $\Delta\text{CTE}$  mismatch it is expected that the residual stresses acting on the fiber matrix interface will be higher in the lead-quartz system. This seems to suggest that there is some relationship between the measured threshold stress and the radial residual stress in the composite system. This is indeed shown to be the case by the model developed in Chapter VI. This suggests that at least for multi-component systems with a large  $\Delta\text{CTE}$ , an alternate source of any measured threshold stress is traceable to the internal residual stress state.

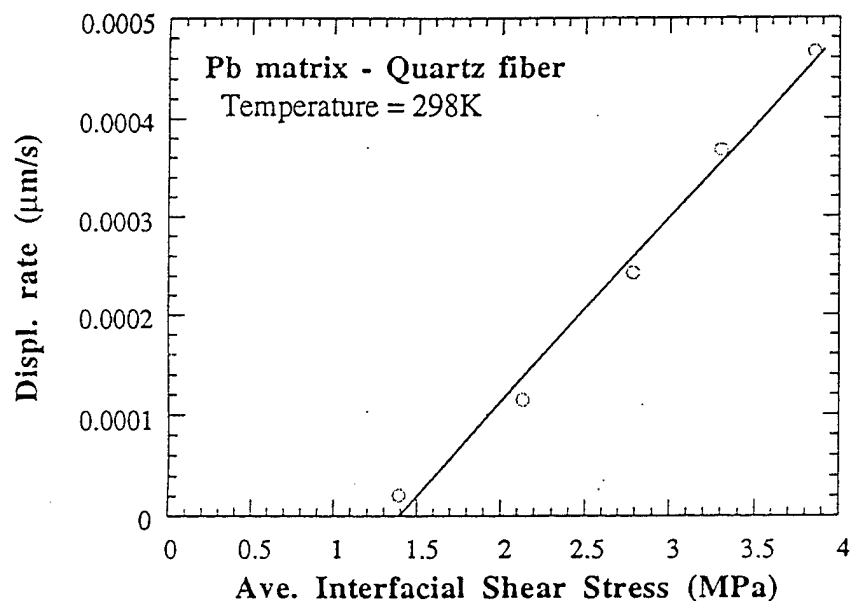


**Figure 26.** Fiber-top displacement corresponding to secondary stage creep (apparent steady state) as a function of the applied average interfacial shear stress for the lead-quartz composite system. The system exhibits a linear stress dependence with a threshold stress of 1.4 MPa.

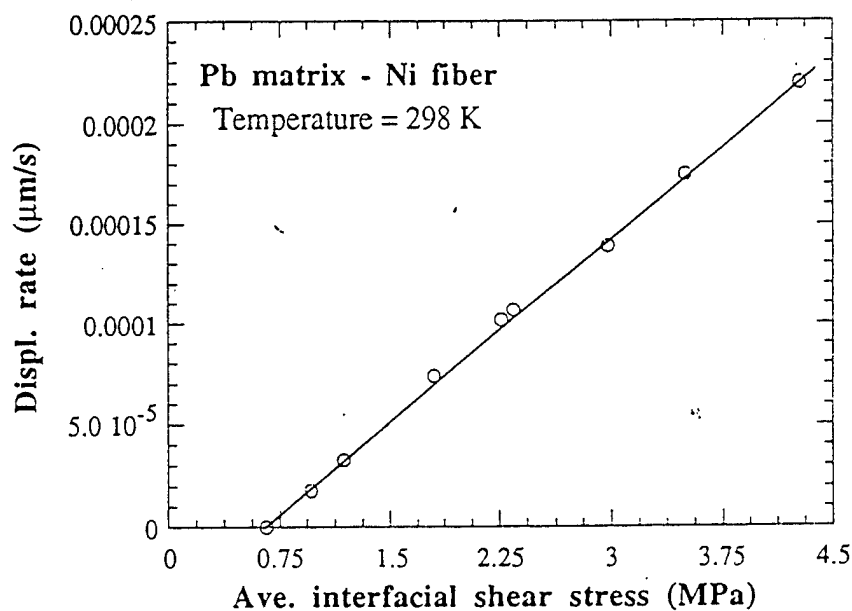


**Figure 27.** Fiber-top displacement corresponding to secondary stage creep (apparent steady state) as a function of the applied average interfacial shear stress for the lead-nickel composite system. The system exhibits a linear stress dependence with a threshold stress of 0.7 MPa.



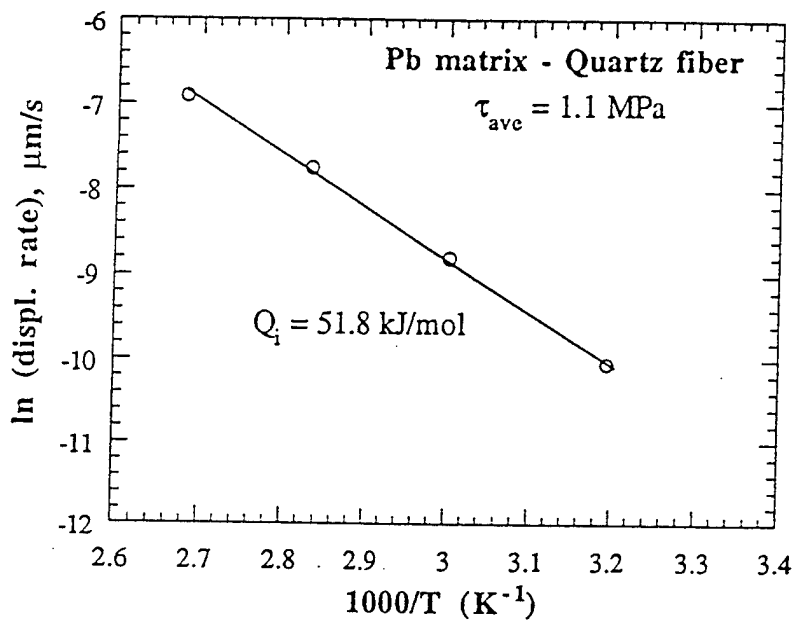


**Figure 28.** Temperature dependence of the interfacial creep rate for the lead-quartz composite system. Tests were conducted at an average applied interfacial shear stress of 1.0 MPa. The activation energy for the interface creep mechanism is calculated to be 51.8 kJ/mol. Note that  $Q_i$  was calculated assuming a constant value for  $\tau_0$ .

## **V. EVALUATION OF THE VALIDITY OF THE EXPERIMENTAL APPROACH: FINITE ELEMENT MODEL**

### **A. PURPOSE**

A finite element approach was utilized in order to evaluate the shear and radial stress distributions in the matrix adjacent to the interface of the single fiber composite (SFC). The purpose of this study was to estimate the spatial variation of the interfacial shear stress during creep testing in a fiber push-out apparatus so that some physical basis may be ascribed to the average interfacial shear stress term used in the representation of the experimental data ( $\tau_{ave} = F/2\pi rt$ ). Further, the FEM approach was used to arrive at an optimum sample design in order to minimize the variation of the interfacial shear stress along the fiber-matrix interface. A further goal of the study was to estimate the radial stresses that develop at the interface due to (a) differential thermal contraction of the matrix and the fiber following cooling from the fabrication temperature, and (b) Poisson expansion of the fiber under the applied load during creep testing. Finally, the FEM approach was utilized to evaluate the contribution of matrix creep on the overall fiber-top displacements measured during the experiments.

### **B. APPROACH**

The axi-symmetry of the SFC allowed the use of a cylindrical coordinate system, with only one-half of the system necessary to be modeled. Displacement-based boundary conditions, with displacements  $u_z$  and  $u_r$  corresponding to the  $z$  and  $r$  axes, respectively, were specified. A schematic of the model is shown in Figure 29. Because of axi-symmetry, all displacements  $u_r$  on the  $z$ -axis were zero, as were all  $u_\theta$  for the entire model.

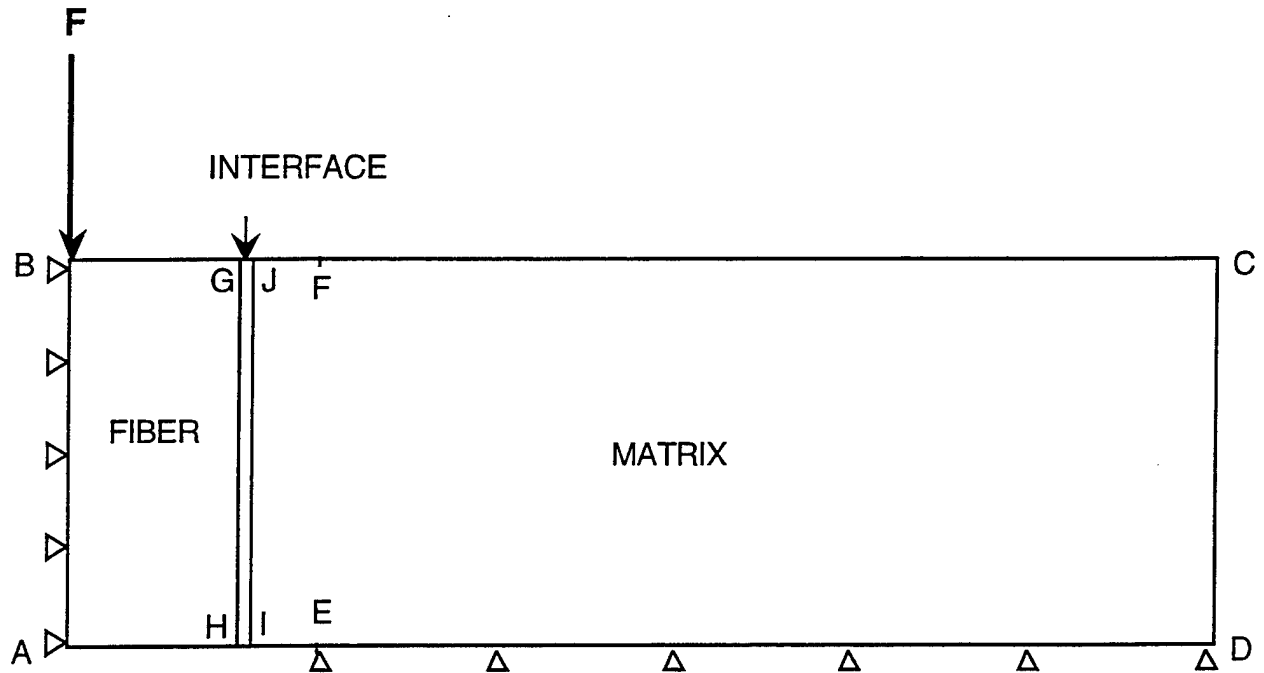


**Figure 29.** Schematic representation of the finite element model of the SFC sample used in the pushout/creep tests.

Additionally, the displacements  $u_z$  of all the nodes on the top surface of the fiber were slaved to the node at  $r=0$ , to which the pushout / creep load was applied. The bottom nodes on the segment ED were constrained in the  $z$  direction, since they rested on the base-plate. As in the experiments, the segment AE, representing the radius of the hole in the base plate, was assumed to be 1.5 times the fiber diameter.

The fiber (Ni) was modeled as an elastic-plastic solid, whereas the matrix (Pb) was modeled as an elasto-plastic creeping solid. Analyses were conducted with two separate assumptions of matrix creep law: (1) dislocation core diffusion controlled power-law creep or (2) grain boundary diffusion controlled diffusional flow (Coble creep) with a matrix

grain size of 5  $\mu\text{m}$  (this number severely underestimates the matrix grain size and therefore exaggerates the matrix creep rate, and was deliberately chosen to conclusively eliminate the possibility that the interface displacements measured in the experiments are influenced appreciably by artifacts due to matrix creep). The relevant data for creep of Pb for both conditions were obtained from Frost and Ashby [Ref. 39].

The "interface" was modeled as a thin region surrounding the fiber. The ratio of its thickness to the fiber radius was assumed to be 0.1. The interface possessed the same elastic and plastic properties as the Pb-matrix, but followed an interface diffusion controlled diffusional flow law as determined experimentally. The relevant constants in the equation were estimated from the experiments and were in qualitative agreement with the explicit equation developed in the next chapter. Appropriate boundary conditions were specified to maintain the verticality of the left and right 'surfaces' (GH and IJ) of the interface. This was done in order to force the interface to strictly follow the contour of the fiber.

The thickness of the SFC sample was varied from a minimum of 1mm to a maximum of 3 mm in order to establish the impact of specimen thickness on the experimental results. The diameter of the SFC sample analyzed was 10mm, which was roughly the same as that used in the experiments. In order to estimate the magnitude of the thermal residual stresses in the radial direction, a steady state thermo-elasto-plastic-creep analysis was conducted whereby all the nodes were cooled simultaneously from 543K to 298K over a period of 4 hours (corresponding to the experimental cooling time following SFC fabrication), after placing it on the base-plate for push-out / creep testing. The matrix yield stress data as a function of temperature were inputs for this part of the analysis.

All analyses were conducted using the multi-physics finite element code ANSYS™.

Analyses was conducted for both the Pb-Ni and Pb-Quartz SFC systems, but only the data for Pb-Ni are reported here.

## **C. RESULTS**

### **1. Effect of Sample Thickness**

The effect of sample thickness on the interfacial shear stress is evident from Figure 30, which shows iso-stress-range regions in the near interface regions of the analyzed model. On the left of the model is the fiber, and the matrix is on the right. The interface is represented by a layer of finely gridded region (3 elements across). In both models, representing 1mm and 3mm thick samples, respectively, the applied load corresponded to an average interfacial shear stress of 2 MPa at 298K. The plots represent the shear stress distribution immediately upon applying the load.

It is clear that the interfacial shear stress varies widely (from negative at the top to positive at the bottom) in the thin sample. With an increase in sample thickness, however, the variation becomes much less, with the majority of the interface now being subjected to a relatively narrow range of shear stresses. Of note is the apparent singularity at the bottom face of the SFC sample, which arises due to the radial tension imposed due to the applied bending moment on the sample. Clearly, this moment, and hence the magnitude of the stress singularity will decline with a decrease in the effective span of the specimen, represented by the diameter of the hole in the base plate, and an increase in the specimen thickness.

It is thus evident that the greater the specimen thickness and the smaller the hole in the base-plate, the more uniform is the distribution of the shear stress along the interface,

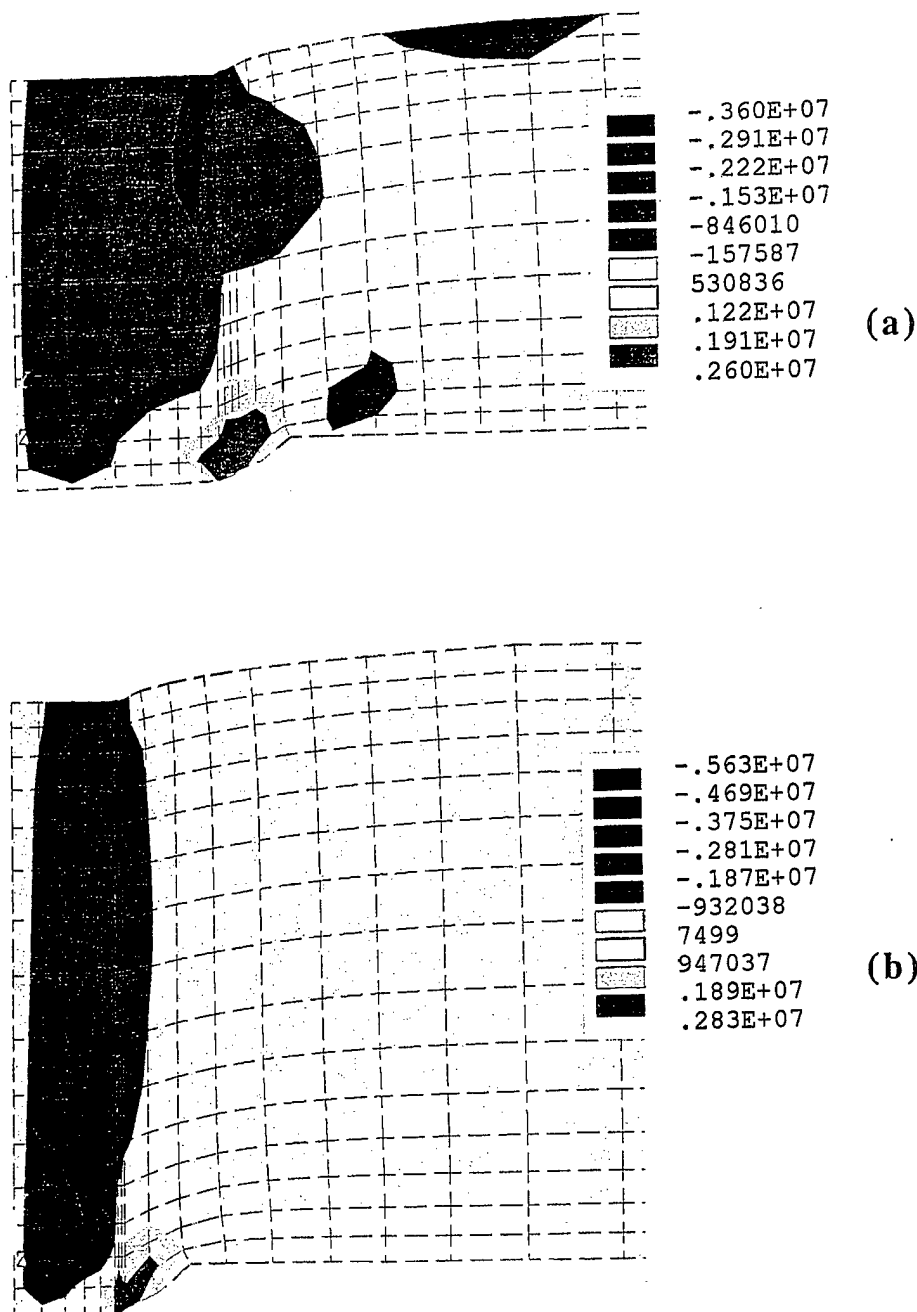


**Figure 30.** Results of FEM analysis showing the effect of sample thickness on the shear stress distribution at the fiber matrix interface. Plot (a) shows the effect of applying a 6N load (corresponding to  $\tau_{ave} = 2$  MPa) on a 1mm thick sample ( $T=298$  K). Note, there is a widely varying shear stress distribution. The 3mm sample shown in plot (b) has a more uniform shear stress distribution with an 18N load ( $\tau_{ave} = 2$  MPa) on the top of the fiber.

and the more meaningful are the experimental results.

## **2. Radial Stresses at the Interface**

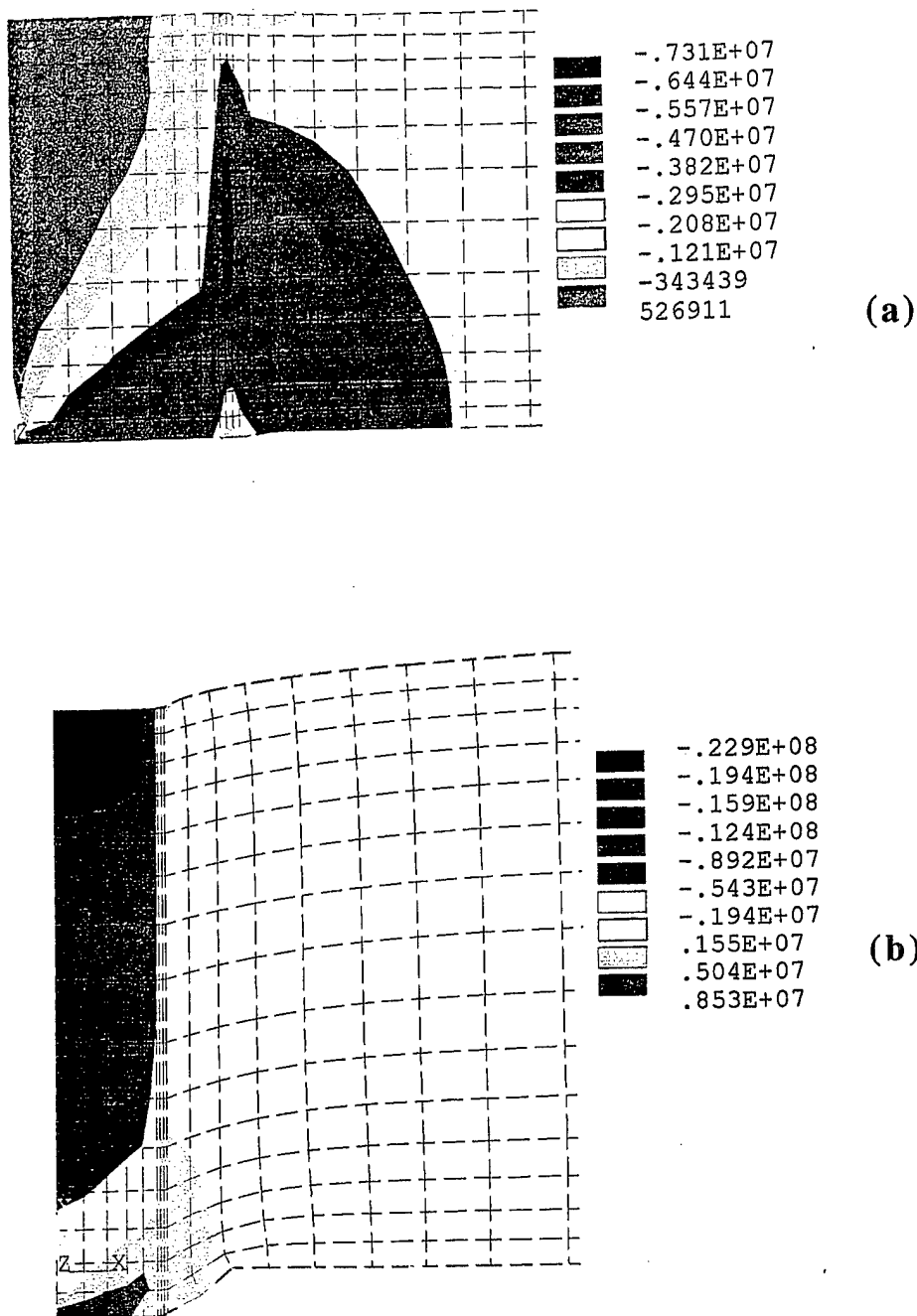
Figure 31a shows the thermal residual radial stress distribution in a 1mm thick SFC sample following cooling from the fabrication temperature. As expected, large compressive stresses are present at the interface. These stresses taper off with increasing distance from the fiber-matrix interface. The magnitude of the peak interfacial radial stresses is observed to be about 7.3 MPa from Figure 31a.

Figure 31b shows the radial stress distribution due to Poisson expansion of the fiber under the applied pushout / creep force corresponding to an average interfacial shear stress of 2 MPa. The radial stress at the interface is observed to lie between -1.9 and 1.5 MPa. It is thus clear that the major contribution to the interfacial radial stresses arises out of thermally generated residual stresses, with a relatively minor contribution from the applied force.

As a rough approximation, we will estimate the interfacial radial stress due to both components (thermal residual and Poisson expansion) to be ~10-11 MPa, which is close to twice the yield strength of the matrix ( $\sigma_{ys} = 5.5$  MPa). This figure will be useful later in estimating the value of the experimentally observed threshold stress based on the analytical model developed in the next chapter.

## **3. Creep strain distribution during Pushout Creep Testing**

In order to check whether the contribution of matrix creep confounds / complicates



**Figure 31.** Results of FEM analysis showing the distribution of radial residual stresses present in the SFC. Plot (a) shows the residual radial stress generated in a 1mm thick sample upon cooling from 543 K to 298 K in 4 hours. Note, the peak radial compressive stress at the interface is roughly 7.3 MPa compressive. Plot (b) shows the radial stresses generated as a result of the Poisson expansion of the fiber under an applied 18N load. Note peak radial compressive stress at the interface is approximately 2 MPa compressive.



the strain rate data obtained during pushout creep testing of SFCs, the creep rate of the matrix was deliberately accentuated by assuming Coble creep with a very small matrix grain size ( $5\text{ }\mu\text{m}$ ), as opposed with an experimentally determined grain size of  $15\text{--}40\mu\text{m}$ ). Additionally, the interface creep rate was deliberately inhibited by assuming that the activation energy for interface creep equals that for grain boundary diffusion (i.e.,  $Q_i = Q_{gb} = 66\text{ kJ/mol.}$ , as opposed to an experimentally determined value of  $Q_i = 52\text{ kJ/mol.}$ ). The finite element model was run for these conditions, assuming 'interfacial amplitude' ( $h/2$ ) values of  $0.1\mu\text{m}$  and  $0.025\mu\text{m}$  (please refer to the next chapter for a physical description of the 'interfacial amplitude'), for total times of 8000 seconds and 1000 seconds, respectively. In both cases, the average interfacial shear stress was 2 MPa, the sample thickness was 3mm, and the test temperature was 298K.

The von Mises effective creep strain distributions are shown for the two situations ( $h = 0.1\mu\text{m}$  and  $0.025\mu\text{m}$ ) in Figures 32a and 32b, respectively. It is quite apparent that even following exaggeration of matrix creep and subduing the rate of interface creep, *all creep strain is confined to the interface for the given applied stress and temperature conditions*. Indeed, analyses showed that within the useful range of applied stresses and experimental temperatures, the interface creep rate was several orders of magnitude larger than the matrix creep rate. This confirms the validity of the experimental measurements (based on the displacement rate of the top face of the fiber) as being representative of interface creep, without confusing artifacts from associated matrix creep.

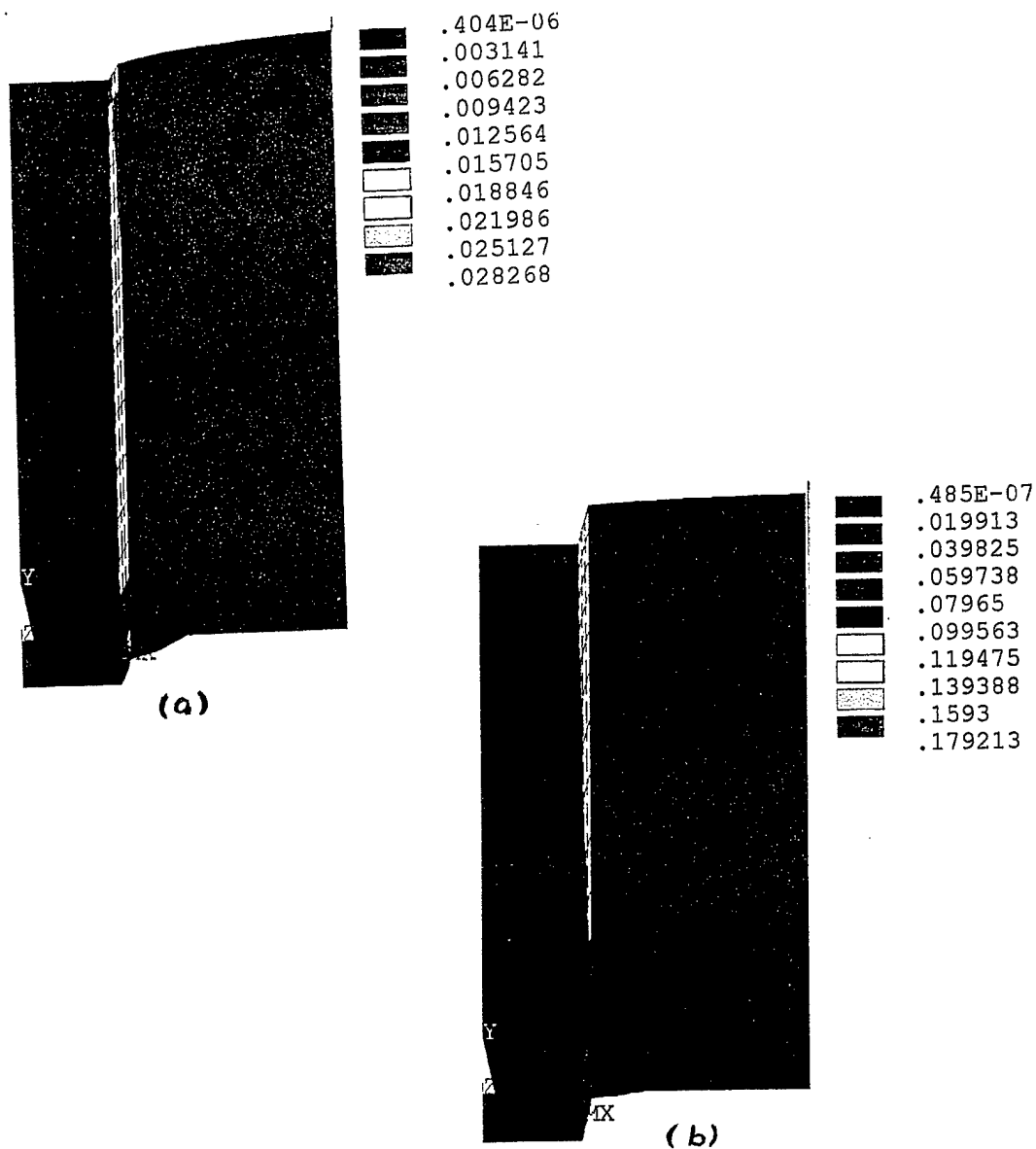


**Figure 32.** Finite element model showing the effect of interface width,  $h$ , on the effective von Mises creep strain distributions. In plot (a),  $h = 0.25 \mu\text{m}$  while in plot (b)  $h = 0.05 \mu\text{m}$ . Note creep strains are confined to the region of the fiber matrix interface.



## VI. MODEL FOR DIFFUSION CONTROLLED INTERFACIAL CREEP

### A. BACKGROUND

The pioneering work by Raj and Ashby [Ref. 40] on diffusional flow controlled grain boundary sliding in polycrystalline materials provides the fundamental insights which are necessary to develop a descriptive model for interfacial sliding in metal matrix composites. Through the course of their experiments they were able to determine that the *shape* of the grain boundary is a controlling factor in the rate of sliding between two adjacent grains. This key observation led to the generation of a sliding model that is controlled entirely through stress-assisted diffusional processes along a nonplanar boundary with a periodically varying normal stress state.

Figure 33 shows four examples of some of the nonplanar periodic boundaries considered by Raj and Ashby. When a shear stress  $\tau_a$  is applied to the periodic boundary, there is an initial instantaneous elastic deformation in the areas where the boundary departs from being a perfect plane. As a result of the elastic accommodation, a distribution of normal stresses is generated along the boundary. This normal stress distribution varies from regions of compression through zero stress to regions of tensile stress. The periodicity of the stress variations is related to the periodicity of the shape of the assumed nonplanar boundary. For temperatures at which the material can undergo creep, the periodic distribution of stress will initiate the diffusive flux of matter from the regions in compression to those under tension. As a result of this diffusive flux the grains on each side of the boundary slide past one another.



diffusional controlled interfacial sliding.

There are two main conditions which will be considered to modify Raj and Ashby's model for the characteristics of the MMC interface. The first issue involves the problem of high levels of radial residual stress at the fiber-matrix interface. As shown in the previous chapter (FEM analysis), the difference in the coefficient of thermal expansion between the fiber and the matrix can result in high levels of radial residual stress at the interface upon cooling from fabrication temperatures. Where Raj and Ashby solely considered the effect of an applied shear stress on the boundary, this model will incorporate the effect of a far-field radial stress normal to the global plane of the periodic boundary. As in the original model, the periodicity of the radial stress contribution is related to the periodicity of the assumed shape of the boundary. The second issue considered must be the effect of the differing material properties between the fiber and matrix. Specifically, since the reinforcing fibers in MMCs typically have a significantly higher melting temperature than the surrounding matrix material, it is usually assumed that the matrix can undergo creep processes while the fiber deforms elastically. Thus, where Raj and Ashby took into account the effect of diffusional flow of matter along the interface and as well through grains on both sides of the boundary, this model only allows for diffusional transport along the interface and through the matrix, (but not through the fiber).

### **C. THE MODEL**

For simplicity, the fiber-matrix interface is characterized as a sinusoidal periodic boundary which can be described by the function,  $x$ :

$$x = \frac{h}{2} \cos \frac{2\pi}{\lambda} y \quad (1)$$

where,  $h$  is the peak-to-peak height (twice the amplitude) of the boundary, and  $\lambda$  is the period of variation along the boundary. Figure 34 (a) shows the resulting form of the boundary as a function of  $y$  ( $y$  being the interface boundary central axis).

When a shear stress is applied on the interface, fiber and matrix the interface undergo initial elastic deformation. The elastic shear accommodation combined with the periodic nature of the boundary results in an entirely normal stress distribution,  $\sigma_{n1}$  along the interface which has the form [Ref. 40]:

$$\sigma_{n1} = -\frac{\tau_a \lambda}{\pi h} \sin \frac{2\pi}{\lambda} y \quad (2)$$

where,  $\tau_a$  is the applied shear stress. Thus, the normal stress distribution varies periodically along the interface from compressive through zero to tensile levels of stress. Figure 34b shows the normal stress distribution in relation to the boundary shape function. Note, there is a  $\pi/2$  phase shift between the normal stress distribution and the assumed boundary shape, although the period of the stress variation is equal to the wavelength of the interface.

For the case of metal-matrix composites, it is well established that high levels of radial residual stresses are generated near the interface due to the difference in the coefficient of thermal expansion between the fiber and matrix. In order to take this effect

into account in the creep model, a far field radial stress is applied on the interface normal to the central boundary axis. Again, due to the periodic nature of the boundary, the distribution of the far field radial stress along the interface is also periodic. However, the radial stress distribution has a period half that of the normal stress distribution. Therefore,  $\sigma_{n2}$  has the form  $\sigma_R \cos^2 \theta$ , where  $\sigma_R$  is the radial stress acting on the fiber-matrix interface, and  $\theta$  is the inclination of the boundary with respect to the y-axis at any point. Here  $\theta$  is assumed to be small (i.e.  $h/\lambda \ll 1$ ) such that  $\sin \theta \approx \tan \theta = dx/dy$ . Therefore,  $\sigma_{n2}$  may be written as:

$$\sigma_{n_2} = \frac{\sigma_R}{2} \left[ \left( \frac{\pi h}{\lambda} \right)^2 \cos \frac{4\pi}{\lambda} y + \left( 2 - \left( \frac{\pi h}{\lambda} \right)^2 \right) \right] \quad (3)$$

This stress distribution is shown in figure 34c. It is clear that  $\sigma_{n2}$  has a location dependent

$$\text{term } \sigma'_{n_2} = \frac{\sigma_R}{2} \left( \frac{\pi h}{x} \right)^2 \cos \left( \frac{4\pi}{\lambda} y \right) \text{ and a location independent term } \sigma''_{n_2} = \frac{\sigma_R}{2} \left[ 2 - \left( \frac{\pi h}{x} \right)^2 \right].$$

The periodic variation of stress along the boundary generates stress induced chemical potential gradients which promote the diffusion of matter from regions under compression to regions under tension. Once the stress state is defined, in order to determine the exact positional variation of the stress induced chemical potential, it is necessary to solve the conservation of mass equation. The conservation of mass condition may be represented as a Laplacian:

$$\nabla^2 \mu(x, y) = 0$$



where  $\mu$  is the point dependent chemical potential.

The boundary conditions necessary to solve this equation are:

$$\begin{aligned}\mu(0, y) &= \mu_o - \Omega(\sigma_{n_1}(y) + \sigma_{n_2}(y)) \\ &= \mu_o - \Omega(\sigma_{n_1}(y) + \sigma'_{n_2}(y) + \sigma''_{n_2})\end{aligned}$$

$$\mu(\infty, y) = \mu_o - \Omega\sigma''_{n_2}$$

$$\frac{\partial \mu}{\partial y}(0, \frac{\lambda}{4}) = 0$$

$$\frac{\partial \mu}{\partial y}(0, \frac{5\lambda}{4}) = 0$$

where:  $\Omega$  is the atomic volume

$\mu_o$  is the chemical potential in the stress free system

$\sigma'_{n_2}$  is the y dependent component in the far field radial stress distribution.

$\sigma''_{n_2}$  is the constant y independent component of the radial stress distribution.

The solution of the conservation of mass equation with the above boundary conditions is:

$$\mu(x, y) = \mu_o - \Omega A \cos \frac{2\pi}{\lambda} (y - \frac{\lambda}{4}) e^{-\frac{2\pi x}{\lambda}} + \Omega B \cos \frac{4\pi}{\lambda} (y - \frac{\lambda}{4}) e^{-\frac{2\pi x}{\lambda}} \quad (4)$$

$$\text{where:} \quad A = -\frac{\tau_a \lambda}{\pi h} \quad \text{and} \quad B = \frac{\sigma_R}{2} \left( \frac{\pi h}{\lambda} \right)^2$$

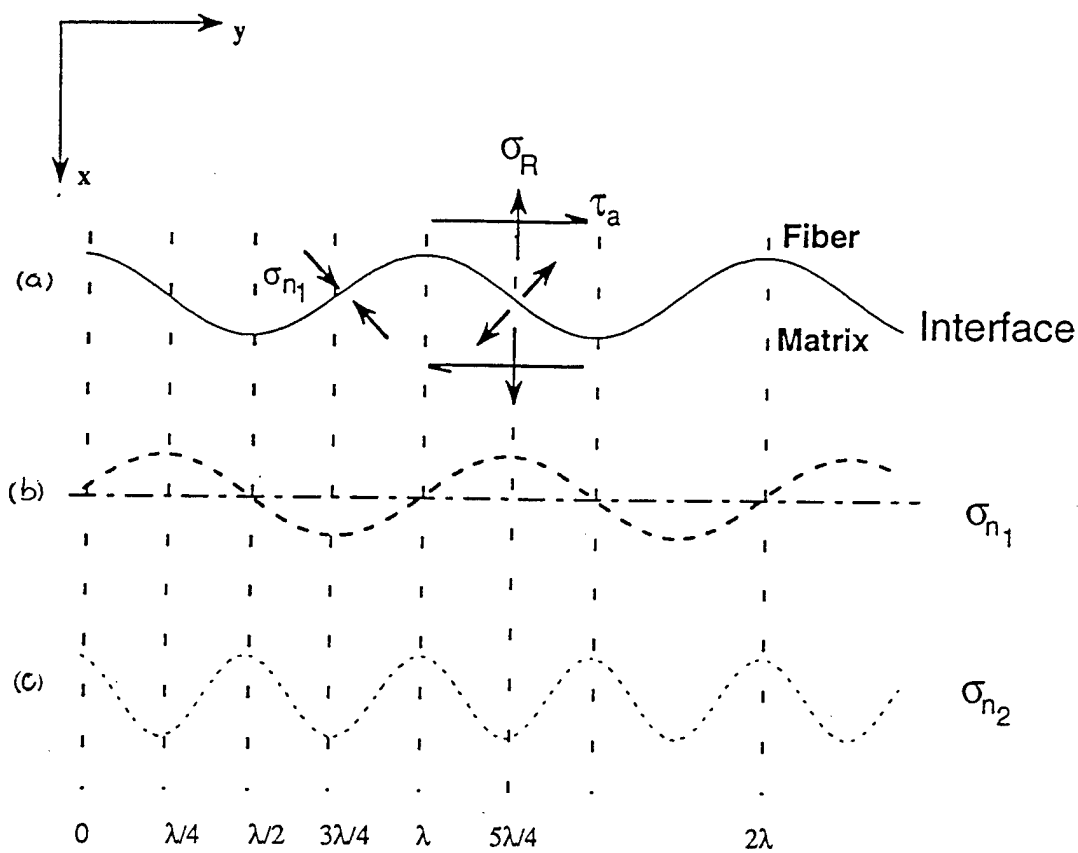


**Figure 34.** Details of the assumed interface shape and stress distribution utilized in developing the model.

- (a) Graphical representation of the nonplanar interface boundary
- (b) Distribution of normal stresses along the boundary following the application of a shear stress
- (c) Distribution of normal stresses along the boundary resulting from the presence of a radial residual stress. Note that the period of  $\sigma_{n2}$  is half that of  $\sigma_{n1}$ .

Figure 35 shows the interface boundary mass flux conditions adapted from the original model proposed by Raj and Ashby [Ref. 40]. As discussed earlier, this model modifies the mechanism proposed by Raj and Ashby. The first modification was the addition of the contribution of the residual stress. The second modification, shown in Figure 35, assumes that there is no diffusional transport of matter through fiber. Thus, the diffusive flux normal to boundary differs from Raj and Ashby in that there is only normal flux into the matrix and none occurs from the boundary into the fiber. Using the approximation that the slope of the boundary  $\sin \theta \approx \tan \theta = (dx/dy)$ , the equation of continuity is defined as:

$$J_m^x(0,y) - \delta_i \left( \frac{\partial J_i^y}{\partial y} \right) = \frac{\dot{U}}{\Omega} \frac{dx}{dy} \quad (5)$$

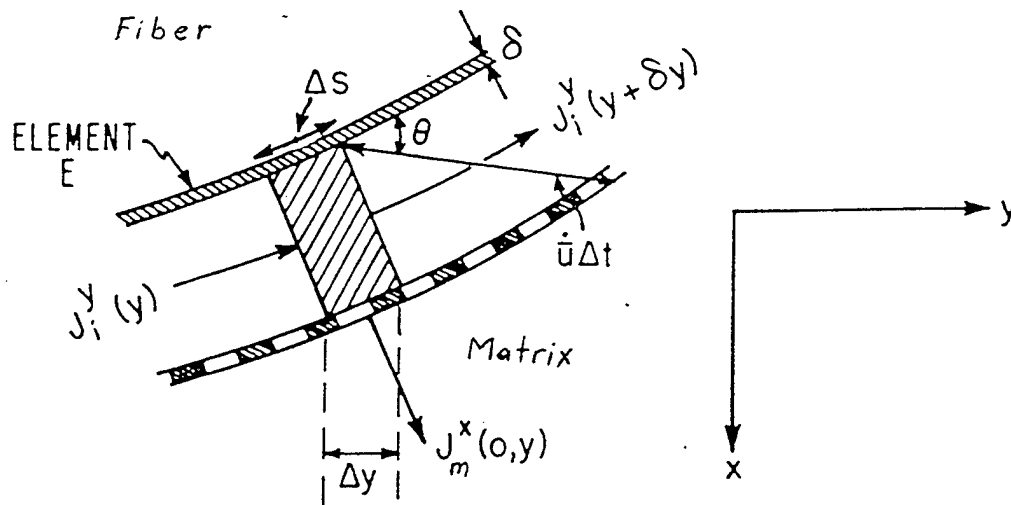


**Figure 35.** Details of an element E, on the interface boundary. Vacancies enter and leave the element via an interface flux  $J_i$ , and a flux through the matrix  $J_m$  [Ref. 37].

where, 
$$\mathbf{J}_m^x = -\frac{D_m}{\Omega kT} \frac{\partial \mu(x,y)}{\partial x} \quad \text{and} \quad \mathbf{J}_i^y = -\frac{D_i}{\Omega kT} \frac{\partial \mu(x,y)}{\partial y},$$
  $D_m$

is the matrix diffusivity,  $D_i$  is the interface diffusivity and  $\bar{U}$  is the average interfacial

sliding rate along the y-axis. Substituting equation (4) into equation (5), and determining the solution at  $y = \frac{n\lambda}{4}$  (where  $n = \text{odd integer}$ ) yields the general form of the constitutive equation for interfacial sliding rate (i.e. creep),  $\dot{U}$ :

$$\dot{U} = \frac{2D_m^{\text{eff}}\Omega\lambda}{kT\pi h^2} \left[ \tau_a + \sigma_R \left( \frac{\pi h}{\lambda} \right)^3 \right] + \frac{4\pi\delta_i D_i \Omega}{kT\pi h^2} \left[ \tau_a + 2\sigma_R \left( \frac{\pi h}{\lambda} \right)^3 \right] \quad (6)$$

Notice that the displacement rate has two components. The first component is associated with diffusion in the matrix, while the second component controlled by diffusion along the interface. Frost and Ashby [Ref. 39] have noted that the activation energy for volume diffusion in lead is high (109 KJ/mol) and the frequency factor  $D_0$  for volume diffusion in Pb is low. Therefore, at least for the experimental system (Pb matrix), the first term is expected to be small. The interfacial sliding rate is therefore likely to be controlled by interface diffusion and  $\dot{U}$  may be written simply as:

$$\dot{\bar{U}} = \frac{4\delta_i D_i \Omega}{kTh^2} \left[ \tau_a + 2\pi^3 \left( \frac{h}{\lambda} \right)^3 \sigma_R \right] \quad (7)$$

The form of this creep law agrees with the creep characteristics proposed observed from the experimental results. Recall, from the experiment, it was observed that  $\bar{U}$  has the general form :  $\dot{\bar{U}} = K(\tau - \tau_o)D_i$ . From equation 7, it is clear that a compressive (negative)  $\sigma_R$  manifests itself as a threshold stress for interfacial sliding, with  $\tau_o$  (the threshold stress) being given by  $\tau_o = 2\pi^3 \left( \frac{h}{\lambda} \right)^3 \sigma_R$

## D. RESULTS

### 1. Threshold Stress Determination

In order to check the correlation between the experimental observations and the analytical result, the expression:

$$\tau_o = 2\pi^3 \left( \frac{h}{\lambda} \right)^3 \sigma_R \quad (8)$$

is used to determine the value of the threshold stress. The value of  $\sigma_R$  is obtained from the results of the finite element study on the lead-nickel composite system.

In the above equation ( $h/\lambda$ ) for the interface is an unknown which needs to be determined by quantitative electron microscopy. Since such experiments were not performed, a reasonable value of ( $h/\lambda = 0.1$ ), is assumed for the following calculations. From the FEM analysis reported in the previous chapter, it was determined that  $\sigma_R$  could reach appreciable levels on the order of twice the yield strength for lead. Therefore, in our case,  $\sigma_R \approx 11$  MPa. Thus, the threshold stress is predicted to be:

$$\tau_o = 2\pi^3 \left( \frac{h}{\lambda} \right)^3 \sigma_R = 2\pi^3 (0.1)^3 \times 11 = 0.682 \text{ MPa}.$$

This predicted value of the threshold stress is very close to the experimentally determined threshold stress  $\tau_o = 0.7$  MPa. Although a FEM analysis was not performed on the lead-quartz composite system, due to the higher mismatch between the coefficients of thermal expansion of Pb and quartz, it is expected that the residual radial stresses generated would be significantly higher than in the lead-nickel system. In accordance with equation (7), the magnitude of the threshold stress increases as the magnitude of the compressive radial residual stress,  $\sigma_R$ , increases. This result is therefore in qualitative agreement with experimental observations in which the threshold stress for the lead-quartz system was found to be approximately 1.5 MPa.

## 2. Estimation of $h$ and $\lambda$

Equation (7) can also be used to gain insight into the geometric factors that characterize the nonplanar boundary. Assuming that the sinusoidal variation of amplitude ( $h/2$ ) and wavelength  $\lambda$  is a good general approximation for the periodic nonplanar boundary, then the curves shown in Figure 36(a and b) can be utilized to determine the amplitude of the boundary variation. The plot shown in Figure 36a is generated from equation 8:

$$\tau_o = 2\pi^3 \left( \frac{h}{\lambda} \right)^3 \sigma_R.$$

The curves shown, represent lines of constant radial residual stress. Once the value of  $\tau_o$  is determined by conducting creep experiments, and the magnitude of  $\sigma_R$  is estimated (e.g. , based on FEM studies, the value of  $h/\lambda$  for the interface may be obtained directly from Figure 36a. Conversely, by assuming a reasonable value for  $h/\lambda$ , Figure 36a can be utilized to estimate the magnitude of the radial residual stress.

In Figure 36b, the functional relationship is obtained by dividing the interfacial sliding rate (equation 7) by the value of the applied shear stress ( $\tau=\tau_a$ ). By plotting the resulting expression as a function of  $h$ , based on equation 7 the variation of  $\dot{U}$  versus  $h$  for various stress ratios ( $\sigma_R/\tau_a$ ) are generated. The interfacial sliding rate and the applied shear

stress are measured from a series of creep experiments. Again,  $\sigma_R$  may be estimated via FEM analysis or through the use of a curve such as that shown in Figure 36a. Then, based on the known quantities the values of

$$\frac{\dot{U}}{\tau_a} \text{ and } \frac{\sigma_R}{\tau_a},$$

it is possible to estimate the value of  $h$  from Figure 36b. These curves, therefore, can be employed to give useful insight into the scale of the periodic variations that influence the rate of diffusional creep along the interface.

Thus, the utility of Figures 36a and 36b lies in the fact that if any four of the six quantities  $\dot{U}$ ,  $\tau_a$ ,  $\tau_o$ ,  $\sigma_R$ ,  $h$  and  $\lambda$  are known, the other two can be directly determined for a known set of material properties ( $\partial_i$ ,  $D_i$ ,  $\Omega$ ) and temperature ( $T$ ). Of the six variables above,  $\dot{U}$ ,  $\tau_o$  and  $\tau_a$  are directly determinable from experiments, and  $\sigma_R$  may be estimated easily via FEM, thereby yielding the means of calculating  $h$  and  $\lambda$ .

From the experimental measurements on the Pb-Ni system, we observe that  $\dot{U}=8 \times 10^{-5} \mu\text{m/s}$  at a  $\tau_a = 2 \text{ MPa}$ ,  $\tau_o \approx 0.7 \text{ MPa}$ , and  $\sigma_R$  (estimated from FEM analysis)  $\approx 11 \text{ MPa}$ . Using these values in conjunction with Figures 36a and b, we estimate that  $h=0.185 \mu\text{m}$  when  $h/\lambda = 0.1$ . These values are not unreasonable for the model system, which suggests that the basis of the analytical model is fundamentally sound.



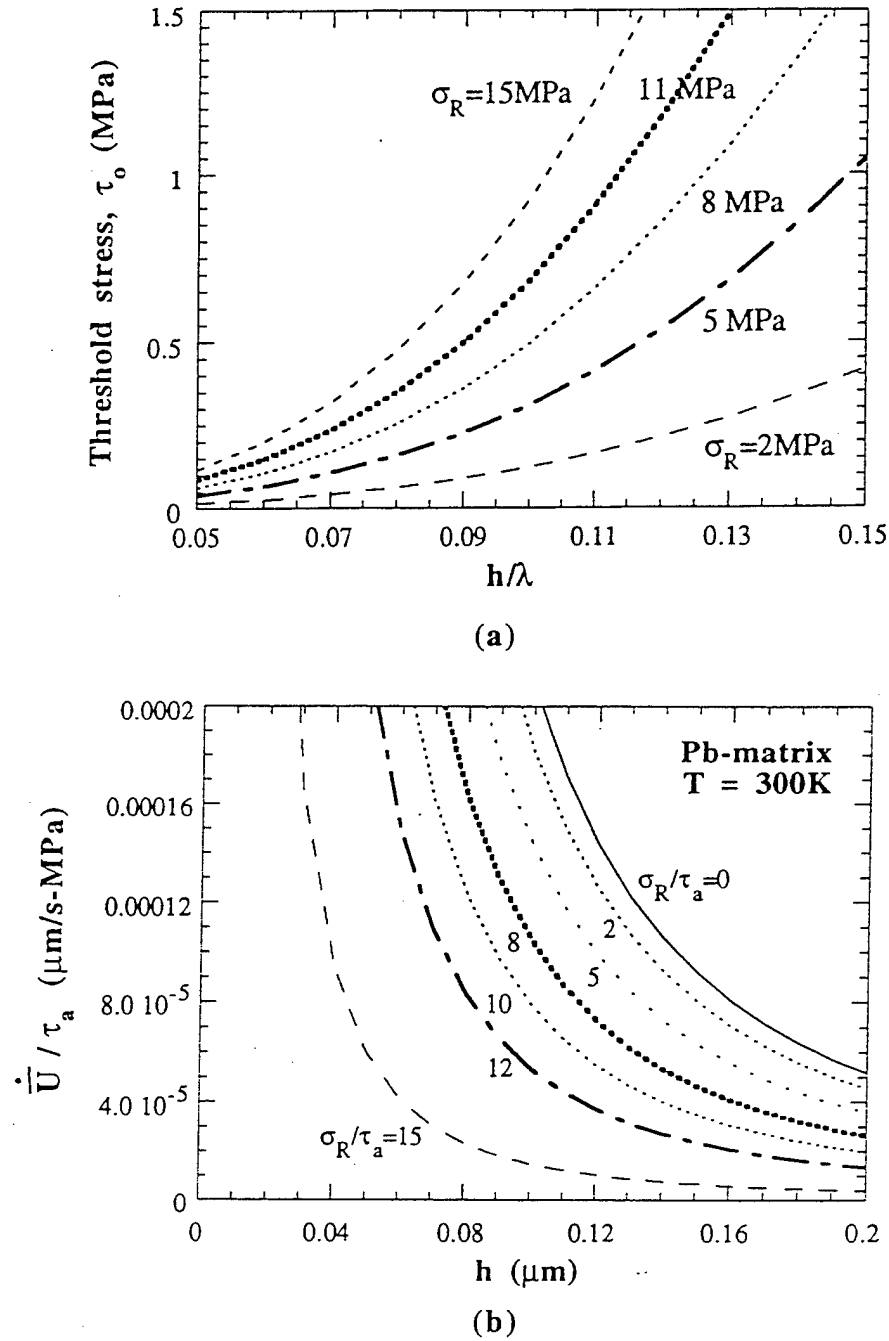


**Figure 36.** Plot (a) shows the magnitude of the threshold stress as a function of  $h/\lambda$ , for various values of residual radial stress  $\sigma_R$ . Plot (b) shows the value of  $\dot{U}/\tau_a$  as a function of the boundary width,  $h$ , for various values of  $\sigma_R/\tau_a$ .

## VII. CONCLUSIONS

1. It has been shown that an indentation / fiber pushout creep approach may be utilized to study the interface creep response of continuous fiber composites. This method is valid as long as the following conditions are satisfied:
  - a. The Young's modulus of the fiber must be much larger than that of the matrix ( $E_f \gg E_m$ ). This stipulation is required in order to avoid complications associated with strongly position dependent shear-lag between the matrix and fiber during the pushout creep experiments, which would result in a large interfacial shear stress variation along the length of the fiber.
  - b. The thickness of the pushout / creep sample must be large in comparison to the fiber diameter and the opening in the base plate, in order to minimize bending moments on the sample due to the applied point loading on the fiber top and thereby, to ensure a uniform shear stress distribution along the interface.
2. The fiber-matrix interface was found to display the following creep properties:
  - a. The kinetics of the interface creep mechanism conform to a linear stress

dependence ( $n=1$ ) which is suggestive of diffusional creep. There is strong experimental and analytical evidence that the measured creep rate is associated with the interface, and not the matrix adjacent to the fiber. The stress dependence was found to be identical for both systems studied, which included lead-quartz, representing a *sharp* interface, and lead-nickel, representing a *diffuse* interface.

- b. Experimental results suggest that there is a threshold stress below which there is no detectible interfacial creep. This threshold stress was found to be higher for the system with a larger thermal contraction mismatch (lead-quartz) and lower for the system with a lower thermal contraction mismatch (lead-nickel).
- c. The activation energy for interfacial sliding in the lead-quartz system was calculated to be less than the activation energy for grain boundary diffusion in lead, and was about half the activation energy for volume diffusion in lead. This suggests that the measured fiber-top displacement is controlled by diffusion along the interface, which, in the lead-quartz system, behaves like a free surface.

3. Raj and Ashby's [Ref. 40] model for diffusional creep controlled grain boundary sliding was modified to account for the effect of imposed radial stresses (generated from the combined effect of thermal residual stresses and Poisson expansion of the fiber)

imposed on the interface. A model describing the kinetics of diffusion controlled interface sliding was thus proposed. The model is capable of explaining the observed threshold behavior entirely on the basis of the interaction of the geometry of the interface with the normal stress (i.e., radial stress) acting on the fiber-matrix interface.

The model provides significant insight on the origin of threshold stresses observed in diffusional creep (Bingham flow), and suggests that this may, at least for multi-component systems with large differences in thermal expansion coefficients ( $\Delta CTE$ ), be attributable to internal thermal residual stresses. The elegance of the model lies in its ability to explain threshold behavior without resorting to complicated dislocation based models for interface control of diffusional creep.



## LIST OF REFERENCES

1. Donomoto, T., K. Funatani, N. Miura and N. Miyake, Ceramic Fibre Reinforced Piston for High Performance Diesel Engines, (1983), SAE paper 830252.
2. Ebisawa, M., T. Hava, T. Hayashi and H. Ushio, Production Process of Metal Matrix Composite (MMC) Engine Block, (1991), SAE paper 910835.
3. Garibotti, J. F., Trends in Aerospace Materials, Astronautics and Aeronautics, (1978), **16**, pp. 70-81.
4. Kelly, A. and K. N. Street, *Creep of Discontinuous Fibre Composites II. Theory for the Steady State*, Proc. R. Soc. Lond. A., (1972), **328**, pp. 283-293.
5. Goto, S. and M. McLean, *Modelling Interface Effects During Creep of Metal Matrix Composites*, Scripta Metallurgica, (1989), **23**, pp. 2073-2078.
6. Goto, S. and M. McLean, *Role of Interfaces in Creep of Fibre-Reinforced Metal-Matrix Composites--I. Continuous Fibers*, Acta Metallurgica et Materialia, (1991), **39**, no. 1, pp. 153-164.
7. Rosler, J., G. Bao and A. G. Evans (1991) *The Effects of Diffusional Relaxation on the Creep Strength of Composites*, Acta Metallurgica et Materialia, **39**, no. 11, pp. 2733-2738.
8. Kim, K. T. and R. M. McMeeking, *Power Law Creep with Interface Slip and Diffusion in a Composite Material*, Mechanics of Materials, (1995), **20**, pp. 153-164.
9. Nimmagada, P. B. R. and P. Sofronis (1996) *Creep Strength of Fiber and Particulate Composite Materials: The Effect of Interface Slip and Diffusion*, Mechanics of Materials, **23**, pp. 1-19.
10. McLean, M. (1985) *Creep Deformation of Metal-Matrix Composites*, Composites Science and Technology, **23**, 37-52.
11. Kelly, A. and W.R. Tyson, *Tensile Properties of Fibre Reinforced Metals-- II. Creep of Silver-Tungsten.*, J. Mech. Phys. Solids, (1966), **14**, pp. 177-186.
12. Matsuura, K., M. Chou and N. Matsuda, *Creep Deformation and Fracture of an Aluminum Composite Reinforced with Continuous Alumina Fibers*, Materials Transactions, JIM, (1991), **32**, no. 11, pp. 1062-1070.
13. Weber, C. H., J. Y. Yang, P. A. Löfvander, C. G. Levi and A. G. Evans, *The Creep and Fracture Resistance of  $\gamma$ -TiAl Reinforced with  $Al_2O_3$  Fibers*, (1993), Acta Metallurgica et Materialia, **41**, no. 9, pp. 2681-2690.
14. Schwenker, S. W. and D. Eylon, *Creep Deformation and Damage in a Continuous Fiber-Reinforced Ti-6Al-4V Composite*, (1996), Metallurgical and Materials Transactions A, **27A**, pp. 4193-4204.
15. Rosler, J., J. J. Valencia, C. G. Levi, R. Mehrabian and A. G. Evans, MRS

Conference, San Francisco, CA, (1990).

16. Dragone, T. L., J. J. Schlautmann, and W. D. Nix, Processing and Creep Characterization of a Model Metal Matrix Composite: Lead Reinforced with Nickel Fibers, *Metallurgical Transactions A*, (1991), **22A**, pp. 1029-1036.
17. Mileiko, S. T., *Steady State Creep of a Composite Material with Short Fibers*, *Journal of Materials Science*, (1970), **5**, pp. 254-261.
18. McDanel, D. L., R. A. Signorelli, and J. W. Weeton, *Analysis of Stress-Rupture and Creep Properties of Tungsten Fiber Reinforced Copper Composites*, (1967), NASA TN-D-4173.
19. McLean, D., *Viscous Flow of Aligned Composites*, *Journal of Materials Science*, (1972), **7**, pp. 98-104.
20. De Silva, A. R. T., *A Theoretical Analysis of Creep in Fibre Reinforced Composites*, *J. Mech. Phys. Solids*, (1968), **16**, pp. 169-186.
21. Bullock, E., M. McLean and D. E. Miles, Creep Behavior of a Ni-Ni<sub>3</sub>Al-Cr<sub>3</sub>C<sub>2</sub> Eutectic Composite, *Acta Metallurgica*, (1977), **25**, pp. 333-344.
22. Dutta, I., S. Mitra and A. D. Wiest, *Some Effects of Thermal Residual Stresses on the Strain Response of Graphite-Aluminum Composites During Thermal Cycling*, *Residual Stresses in Composites*, E.V. Barrera and I. Dutta eds., (1993), pp. 273-292.
23. Yoda, S., N. Kurihara, K. Wakashima, and S. Umekawa, *Thermal Cycling-Induced Deformation of Fibrous Composites with Particular Reference to the Tungsten-Copper System*, *Metallurgical Transactions A*, (1978), **9A**, pp. 1229-1236.
24. Miracle, Daniel B., WL/MLLM, WPAFB, OH, (1997), private communication.
25. Mitra, S., I. Dutta and R.C. Hansen, *Thermal Cycling Studies of a Cross-plyed P100 Graphite Fibre-Reinforced 6061 Aluminum Composite Laminate*, (1991), *Journal of Materials Science*, **26**, pp. 6223-6230.
26. Massalski, T. B., *Binary Phase Diagrams*, Materials Park, OH: ASM International, (1990), pp. 2837-2838.
27. Chandra, N. and C. R. Ananth, *Analysis of Interfacial Behavior in MMC's and IMC's by the Use of Thin-Slice Push-Out Tests*, (1995), *Composites Science and Technology*, **54**, pp. 87-100.
28. Evans, R.W. and B. Wilshire, *Creep of Metals and Alloys*, Swansea: The Institute of Metals, (1985), pp. 88-89.
29. Ghosn, L. J., J. I. Eldridge and P. Kantzos, *Analytical Modeling of the Interfacial Stress State During Pushout Testing of SCS-6/Ti- Based Composites*, (1994), *Acta Metallurgica et Materialia*, **42**, no. 11, pp. 3895-3908.
30. Mukherjee, S., C.R. Ananth and N. Chandra, *Evaluation of Fracture Toughness of MMC Interfaces Using Thin-Slice Push-Out Tests*, (1997), *Scripta Materialia*, **36**, no. 11, pp. 1333-1338.

31. Dollar, A., P. S. Steif, Y.C. Wang and C. Y. Hui, *Analyses of the Fiber Push-Out Test*, (1993), Int. J. Solids Structures, 30, no. 10, pp. 1313-1329.
32. Majumdar, B. S. and D. B. Miracle, *Interface Measurements and Applications in Fiber-Reinforced MMC's*, (1996), Key Engineering Materials, **116-117**, pp. 153-172.
33. Liang, C. and J. W. Hutchinson, *Mechanics of the Fiber Pushout Test*, (1993), Mechanics of Materials, **14**, pp. 207-221.
34. Kallas, M. N., D. A. Koss, H. T. Hahn and J. R. Hellmann, *Interfacial Stress State Present in a "Thin-Slice" Fibre Push-Out Test*, (1992), Journal of Materials Science, **27**, pp. 3821-3826.
35. Watson, M. C. and T. W. Clyne, *The Use of Single Fibre Pushout Testing to Explore Interfacial Mechanics in SiC Monofilament-Reinforced Ti -- II. Application of the Test to Composite Material*, (1992), Acta Metallurgica et Materialia, **40**, no. 1, pp. 141-148.
36. Ashby, M. F., *On Interface-Reaction control of Nabarro-Herring Creep and Sintering*, (1969), Scripta Metallurgica, **3**, pp. 837-842.
37. Ashby, M. F., *Boundary Defects and the Mechanism of Particle Movement Throuth Crystals*, (1969), Scripta Metallurgica, **3**, pp. 843-848.
38. Arzt, E., M. F. Ashby and R. A. Verrall, *Interface Controlled Diffusional Creep*, (1983), Acta Metallurgica, **31**, pp. 1977-1989.
39. Frost, H. J. and M. F. Ashby , *Deformation-Mechanism Maps, The Plasticity and Creep of Metals and Ceramics*, Oxford: Pergamon Press, (1982).
40. Raj, R. and M. F. Ashby, *On Grain Boundary Sliding and Diffusional Creep*, (1971), Metallurgical Transactions, **2**, pp. 1113-1127.





## INITIAL DISTRIBUTION LIST

1. Defense Technical Information Center.....2  
8725 John J. Kingman Rd., STE 0944  
FT. Belvoir, Virginia 22060-6218
  
2. Dudley Knox Library.....2  
Naval Postgraduate School  
411 Dyer Rd.  
Monterey, California 93943-5100
  
3. Naval Engineering, Code 34 .....1  
Naval Postgraduate School  
Monterey, California 93943-5100
  
4. Department Chairman, Code ME/Mc .. .....1  
Department of Mechanical Engineering  
Naval Postgraduate School  
Monterey, California 93943-5000
  
5. Professor I. Dutta, Code ME/Du .....1  
Department of Mechanical Engineering  
Naval Postgraduate School  
Monterey, California 93943-5000
  
6. Dr. Bruce A. MacDonald .....1  
Program Director  
Metal, Ceramics, and Electronic Materials  
National Science Foundation  
Materials Research Division  
4201 Wilson Blvd. Rm. 1065  
Arlington, VA 22230
  
7. Dr. Daniel B. Miracle .....1  
Metallic Composites Research Group Leader  
AF Wright Laboratory  
Materials Directorate  
WL/MLLM Bldg 655  
2230 Tenth St. Suite 1  
WPAFB, OH 45433
  
8. Dr. Wilbur Simmons .....1  
Material Science Division  
U.S. Army Research Office  
P.O. Box 12211  
Research Triangle Park  
North Carolina 27709-2211

9. Dr. Ernest Chin .....1  
Army Research Lab  
AMRSL-MA-MR  
APG, Maryland 21005-5069
10. LT John V. Funn .....2  
3901 Maidens Road  
Powhatan, VA 23139